ChemCatChem

Research Article
doi.org/10.1002/cctc.202201556

Chemistry Europe
European Chemical Societies Publishing

www.chemcatchem.org

Synthesis of Highly Active and Stable Carbon by a Soft-Template Hydrothermal Route as Pt Substrate for Oxygen Reduction Reaction

Jithin Antony,[a] Mariappan Sakthivel,*[a] and Jean-Francois Drillet*[a]

N-doped mesoporous carbon spheres were synthesized by a microwave-assisted ammonia-catalyzed hydrothermal route (C_{FAHM}) by using Pluronic® F127 as a soft-template and *m*-Aminophenol as both carbon and nitrogen source. Their physical and electrochemical properties were compared with those of carbon samples obtained by a conventional hydrothermal method (C_{FAH}). The best results in terms of particle size, surface area, pore size distribution, conductivity and N-content of the as-prepared C_{FAHM} samples were obtained in 17 M NH_4OH at 120 °C for 5 min. After 1100 °C pyrolysis step, conductivity of C_{FAHM} increased to 5.64 S cm^{-1} compared to 8.64 S cm^{-1} for C_{FAH} sample. Remarkably, GDE experiments with xylene-swelled C_{FAHM}-supported platinum exhibited an excellent activity for ORR (181 mA cm^{-2} @ 0.7 V) and ECSA retention (80% after 10,000 ADT) under half-cell conditions in 1 M H_2SO_4 at room temperature compared to only 57 mA cm^{-2} and 13% for GDE with Pt/C_{Vulcan} reference material.

Introduction

Proton exchange membrane fuel cell (PEMFC) is an environmental-friendly energy conversion technology that is supposed to replace combustion engine in some specific fields, such as backup power supply for critical infrastructure and transportation of passengers and goods. PEMFC has several advantages related to low operation temperature (80 °C),[1] fast start-up, high power density, low environmental emissions, relatively high chemical-to-electrical energy conversion efficiency[2] and intrinsic simplicity.[3] However, performance of PEMFC is limited by both sluggish kinetics of electrochemical reduction of twofold-bonded atoms in oxygen molecule and long-term stability of carbon-supported nano-dispersed catalyst. To date, Pt catalysts have shown the highest catalytic activity for oxygen reduction reaction (ORR) among pure metals.[4] Furthermore, some Pt alloys such as Pt_3Co,[5] Pt_3Ni[6,7] and PtCr[8] have been identified as more efficient and stable system due to shift of d-band center[9] and more generally to change in their electronic structure compared to that of pure Pt.[10] In that context, density functional theory (DFT) calculations may help to get a better understanding in composition-dependent synergies for optimization of catalyst composition.[11]

While intrinsic activity of catalyst alone is of great importance, its long-term activity and stability in technical applications is also depending on morphology, porosity and corrosion resistance of the carbon support as well. In the past decades, numerous carbon structures such as CNTs, SWCNT, MWCN, graphene have been developed and tested for low-temperature fuel cells applications.[12] None of them fulfil required properties especially synthesis cost and residual impurities such encapsulated nickel catalyst in MWCNTs might compromise their long-term stability.[13] It is meanwhile accepted that a spherical shape and a mesoporous surface structure can facilitate mass transport of reactants and products within catalyst layer and enhance catalyst confinement, respectively. Ideally carbons with pore size in the range of 15–20 nm and large mesopore area are favorable for formation of highly dispersed Pt particles.[14] Since there is still no similar commercially available product on the market, designing of appropriate carbon structure with environmental-friendly and cheap compounds remains a challenge. Depending on the application field, two distinct options namely hard and soft templating routes can be followed.

Hard templating can help preparing a wide range of materials, in particular highly crystalline and even single-crystal materials due to the resistance of the rigid template to high temperatures. An overview about amorphous and crystalline mesoporous silica nanoparticles is given in references.[15,16,17] In a previous study, we found that ordered mesoporous carbon (OMC) flakes from CMK-3 silica template with pore size in the range of 3.3–5.0 nm strongly prevent agglomeration and degradation of Pt particles during accelerated degradation procedure during half-cell experiments compared to benchmark Pt/Vulcan having a mean pore size of about 2 nm.[18] However, two- dimensional carbon structures cause mass transport limitation and are not suitable for high current applications. Therefore, synthesis of carbon spheres with optimal confine-

[a] J. Antony, Dr. M. Sakthivel, Dr. J.-F. Drillet
Energy Storage and Conversion
DECHEMA-Forschungsinstitut
Theodor-Heuss-Allee 25
60486 Frankfurt am Main (Germany)
E-mail: sakthivel.mariappan@dechema.de
jean.drillet@dechema.de

Supporting information for this article is available on the WWW under https://doi.org/10.1002/cctc.202201556

ment structure is more straightforward.[19] Ajayan et al.[20] successfully synthesized mesoporous carbon nitrides with adsorption and desorption pore size distribution of 4 and 4.2 nm, respectively. Zhang et al.[21] synthesized carbon with pore size of 3.2 nm with F127 as template via hard-template route. They also shown that increase of pyrolysis temperature from 500 to 800 °C leads to reduction of pore size from 3.5 to 3.2 nm. Zhibin et al.[22] synthesized MCNs by using self-synthesized mesoporous silica nanospheres as template and ferrocene as carbon precursor and applying chemical vapor deposition method. Xia et al.[23] synthesized silica templates from Pluronic 123 which was then used for the synthesis of MCNs. Despite its very good capability to synthesize MCNs, this method is time-consuming and not environment-friendly because template etching step by e.g., HF is usually necessary. Moreover, mesostructure and morphology of carbon replicated depends mostly on silica template and therefore is difficult to tune.

Therefore, many works focused on soft-template routes that might circumvent some issues that hard-template methods face. As an organic self-assembly method, template is easily formed and removed compared to e.g., silica material. The complexity is less, and the reaction has good controllability.[24,25] Common precursors are resol, phenol and formaldehyde. Pluronic® F127 is mostly used as template. This method can include either acidic or base-catalyzed polymerization. As a successful example of acidic-catalyzed polymerization, Lu et al.[26] synthesized carbon using glutamic acid as catalyst and resol as precursor with F127 as template whereas Liu et al.[27] choose citric acid as catalyst in combination with the same precursors and template materials. Wei et al.[28] used highly acidic conditions with 2 M HCl to synthesize micro and mesoporous carbon particles of size 0.71 and 2 nm respectively. In our previous work,[29] carbon was yielded via aqueous polymerization by mixing resol with HCL and F127 at 120 °C for 12 h and finally calcinating step by 700–900 °C. Feasibility of a one-pot base-catalyzed hydrothermal synthesis was demonstrated by Wang et al.[30] that relies on ammonia solution as catalyst for polymerization, F127 as template, m-Aminophenol and hexamethylenetetramine (HMT) as precursor. Since resol is formed in-situ, this base-catalyst route appears to be more straightforward than acid-catalyzed multi-step one.

However, soft-template synthesis of carbon via organic-organic self-assembly often resulted in carbon with pore size falling in the micro-mesoporous border region due to shrinkage of the framework while pyrolysis.[21] One of the first study on effect of swelling agents or micelle expanders on pore expanding was published by Han et al.[31] By proper choice of surfactant and swelling agent with adequate hydrophobicity or hydrophilicity, formation of mesoporous carbon with large pores can be facilitated. Kruk et al.[32] has shown that different swelling agents like 1,3,5-triisopropylbenzene, 1,3,5-triethylbenzene and cyclohexane have different solubilization capabilities in the same surfactant Pluronic®123 (P-123) used for synthesis of ultra-large pore silica. Alkyl benzenes with different number of substituted chains were used as swelling agents for soft template Pluronic PEO-PPO-PEO [poly (ethylene oxide) - poly (propylene oxide)-poly (ethylene oxide)] triblock copolymer. It has been founded that as the number of the side chains decreased, the swelling agents were more soluble in the surfactant. The two possible structural description of the interaction between swelling agent and surfactant was calculated by R. Nagarajan.[33] He suggested that the swelling of micelle can be analogous to simple solubilization and micro-emulsification. The first model explains the possibility of the presence of a mixture of swelling agent, hydrophilic blocks at the core region whereas the latter model describes a core region constituting of only pure swelling agent.[33] It is important to monitor solubilization step of swelling agents in the micelles, because high rate of solubilization resulted in disordered and heterogeneous structures.[34] The addition of decane as a swelling agent with the surfactant P-123 during the synthesis caused pore width enlargement of carbons from 11.5 to 14.7 nm.[25] 1,3,5- tri-alkylbenzene was used to obtain ultra-large pore in carbon structure from SBA-15 silicas.[35] The possibility of using hexane,[36] cyclohexane and toluene[32] as swelling agents was also studied. Huang et al.[37] classified xylene as an efficient swelling agent with Pluronic-F127 over 1,3,5-trimethylbenzene for the synthesis of face-centered cubic silica. It is well-known that Pluronic® F127 has only ~30 wt% of hydrophobic PPO chains. This allows a limited intake of xylene and prevents structural deformity. Xylene combines with water-repelling PPO chains in the template is responsible for moderate swelling of the template.[38]

Carbon conductivity and nitrogen content

It has been claimed that graphitic level of carbon can be enhanced by increasing pyrolysis temperature (T_{Py}). A 32-fold improvement in conductivity of carbon from 2.5 up to 80 $S\,cm^{-1}$ was reported when T_{Py} was raised from 800 to 1000 °C, respectively while N content decreased from 9.0 down to 3.9 wt%.[39] Conductivity of various carbon types were reviewed by E. Antolini[14] out of which some are discussed here. Vulcan XC-72R which is turbostratic (micro and mesoporous nature)[40] has shown an electrical conductivity (σ) of 4.0 $S\,cm^{-1}$. On the other hand, ordered mesoporous carbon exhibited a conductivity in the range of 3.3×10^{-2}–1.4 $S\,cm^{-1}$. While carbon nano horns and carbon nano cages which contain mixed micro and mesopore domains have shown conductivity in the range 3–200 $S\,cm^{-1}$, conductivity of up to 102–104 $S\,cm^{-1}$ have been measured at mesoporous carbon nano fibres.

The doping of carbon with heteroatoms like nitrogen, boron and phosphorous have already been reported elsewhere.[41] Nitrogen is one of the best elements for doping as a heteroatom, because of its modest size compared to carbon[42] and high electronegativity ($\chi = 3.04$) compared to that of carbon ($\chi = 2.55$), boron ($\chi = 2.04$) and phosphorus ($\chi = 2.19$).[43] After N-doping, electron accepting nitrogen imparts a high positive charge density on adjacent carbon atoms.[44] By using m-aminophenol as carbon precursor, Liu et al.[45] yielded carbon with 4.3 wt% N. With the help of vapor deposition and using a silicon substrate as the catalyst which was further pyrolyzed at 800 °C, Wei et al.[46] obtained an 8.9 wt% N-doped carbon.

However, thermal stability of nitrogen atoms in carbon framework is very low since N prefers to exist in its molecular form.[40] N can be integrated within C framework that is able to form different carbon nitrides with five different structures predicted so far. One is the two-dimensional graphitic C_3N_4 and the other ones are three-dimensional carbon nitrides namely α-C_3N_4, β-C_3N_4, cubic C_3N_4 and pseudocubic C_3N_4.[47] High temperature pyrolysis results in rather N-doped graphitized carbon than carbon nitrides.[48] The relation between N-content, T_{Py} and conductivity is not fully understood yet. In terms of electrocatalytic aspects, nitrogen atoms improve both surface polarity and electron donor properties of the carbon matrix as well as creation of active basic/catalytic sites on the carbon surface.[49] Zhou et al.[50] yielded nitrogen-doped hollow mesoporous carbon spheres with a particle diameter of about 150 nm and adjustable N-doping levels (3.6–7.8%). Their superior electrocatalytic activity for the oxygen reduction reaction (ORR) was attributed to the high content of graphitic-N and pyridinic-N groups on carbon spheres. Shao et al.[51] reported of N-doped OMCs with high surface areas (923–1374 $m^2 g^{-1}$), large pore volumes (1.32–2.21 $cm^3 g^{-1}$), bimodal mesopores (4.8 nm and 6.2–20 nm) and high nitrogen content (3.6%–12.2%) from the simplest amino acid (Glycine) as carbon precursor by a solvent-free nanocasting method. OMC shows a good ORR performance with a high onset of 0.92 V and a high half-wave potential of 0.83 V. Zhou et al.[52] developed N-modified Pt/C catalyst with 2.32-fold improvement in activity for ORR and higher stability in acid electrolyte. At the same time, N-doping prevented Pt nanoparticles aggregation during the stability tests. Zelenay's group[53] synthesized recently atomically-dispersed Co–N–C (non PGM) catalyst via an encapsulation ligand exchange approach. It exhibited a high catalytic ORR activity in 0.5 M H_2SO_4 and four times enhanced durability compared to that of Fe–N–C catalyst. A detailed study on the degradation mechanisms revealed that the durability enhancement of Co–N–C catalysts was due to lower activity of Co ions for Fenton reaction which prevents interaction of radicals and enhanced resistance to demetallation of Co–N–C.

Microwave-assisted hydrothermal synthesis

Numerous works on microwave radiation influence in the field of synthetic chemistry were carried out during last few decades.[54] In the mid-1980s, it was reported that organic reactions can be accelerated by microwave ovens.[55] Conventional hydrothermal heating methods often resulted in longer reaction time whereas use of microwaves as heating source accelerate reaction rate of polar reactants.[56] On contrary to conventional thermal heating sources, the microwave-assisted method creates local heating spot inside the sample and then radiates it outwards.[57] This does not occur through convection or conduction but through dielectric heating.[58] Materials dissipate microwave energy mainly by two major mechanisms: dipole rotation and ionic conduction. In dipole rotation, the molecules that are permanent or induced dipoles aligns with the electric field component of radiation. During ionic conduction, migration of dissolved ions is generated by oscillating electric field. Heat generation is caused by frictional losses which depend on the size, charge, and conductivity of the ions, and their interactions with the solvent.[56] Microwave-assisted route helps in homogeneous heating in the reaction vessel resulting in homogeneous nucleation and shorter crystallization time.[58] Microwaves were used to synthesis hollow carbon spheres with hierarchical pore size for the application in Li ion batteries were synthesized by Zou et al.[35] and mesoporous carbon support by Chen et al..[59] Bein et al.[58] discussed the possibility of variation of reaction mechanism when microwaves were used for hydrothermal treatment. Porous carbon spheres were prepared through microwave-assisted reaction followed by different thermal treatment at 600, 800 and 1000 °C and it was experimentally proven that the high T_{Py} has shown high electrochemical activity.[60] Microwave-assisted pyrolysis method was used for ultrafast production of ordered mesoporous carbon.[61] Arif et al.[62] used microwave irradiation to fasten the polymerization of 3-aminophenol as carbon source and formaldehyde.

In this work, spherical porous carbon particles were synthesized via microwave-assisted ammonia-catalyzed hydrothermal synthesis. While some parameters for hydrothermal synthesis (FAH) from our previous work such as reaction temperature (RT) of 120 °C and reaction time (RCT) of 12 h were very promising and further used in this work, some other ones like ammonia concentration of 14 M and pyrolysis temperature of 900 °C led to particle agglomeration and insufficient conductivity, respectively.[29] Therefore, the effect of ammonia concentration and influence of pyrolysis temperature (T_{Py}) on electronic conductivity and N-content of carbon samples were studied more in detail in this work. Moreover, influence of xylene as swelling agent on carbon surface area and pore width distribution were explored as well. Finally, Pt catalyst was deposited on carbon and its activity for oxygen reduction (ORR) was evaluated under half-cell conditions at room temperature.

Results and Discussion

Parameter optimization of FAH hydrothermal carbon synthesis

While some parameters such as reaction temperature (RT) of 120 °C and reaction time (RCT) of 12 h were adopted from our previous work,[29] this study focuses on effect of ammonia concentration in the range of 1 to 17 M as well as pyrolysis temperature T_{Py} between 700–1300 °C on carbon morphology.

From the Figure 1a, it can be observed that variation of ammonia concentration at T_{Py} of 900 °C, in which no substantial effect on mean particle size of carbon samples lying in the range of 4.3–5.03 μm. Synthesis with 1 M ammonia obviously led to reaction products with the best particle size distribution around 4.3 μm. On a close observation at 1 and 6 M carbon particles, however, their shape seems to be affected. While 12 M carbon particle shows slightly defective particles, use of 17 M (30 wt%) ammonia resulted in sample with the best

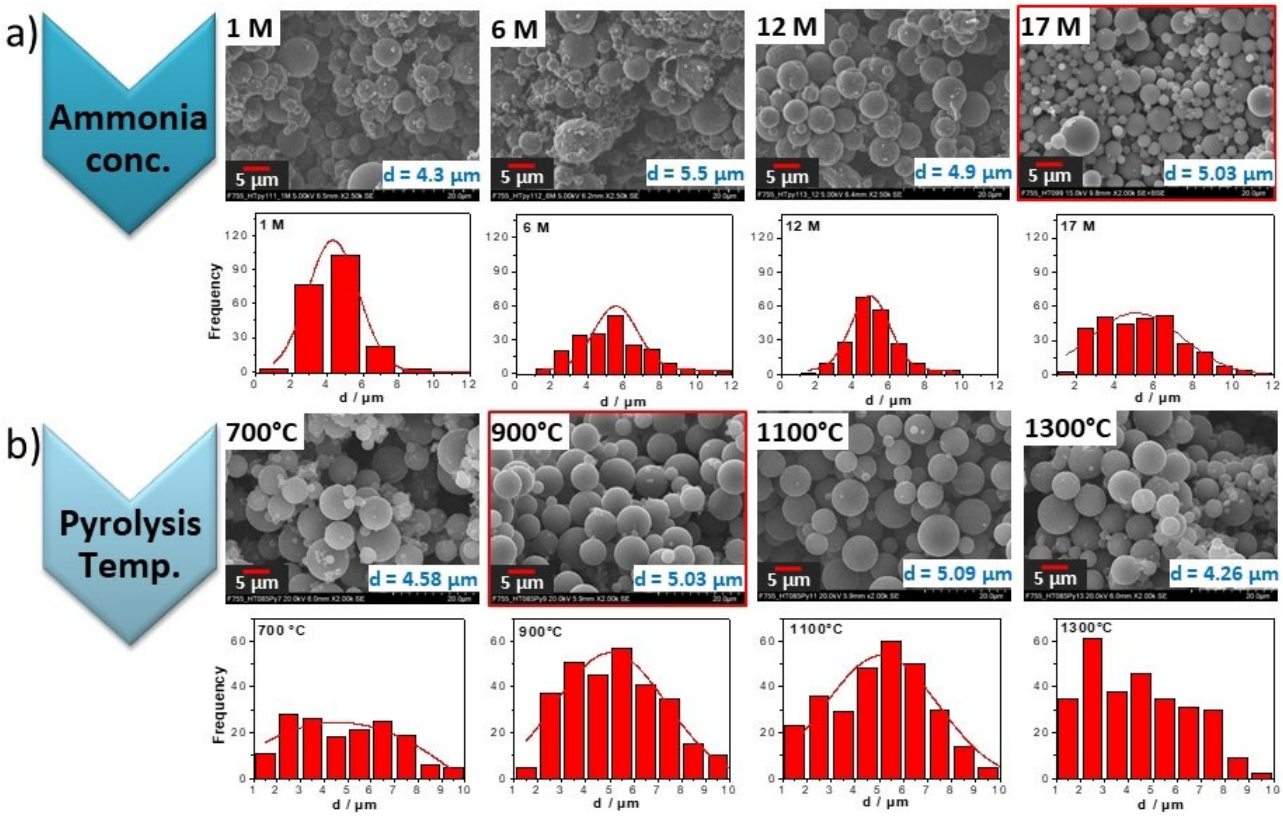

Figure 1. SEM images of C_{FAH} at different a) ammonia concentrations at 900 °C and b) pyrolysis temperatures from 17 M solution.

spherical shape. Wang et al.[30] mentioned the usage of 0.14 M ammonia for their experiments with MAP, HMT and F-127 that affected spherical morphology of carbon spheres using a reflux condition. Since here best results in terms of particle size and shape were yielded with 17 M ammonia catalyst, further T_{Py} optimization was conducted with this concentration. From Figure 1b, the pyrolysis of 17 M polymer samples at T_{Py} from 700 up to 1100 °C resulted in almost similar mean particle size in the range of 4.2–5.5 µm. At T_{Py} = 1300 °C, however, the best mean particle size of 4.26 µm has been measured. This shrinkage can be assigned to loss of formaldehyde and surfactant[38] which eventually formed the framework containing water.

Table 1. Influence of reaction temperature on carbon particle size at constant P, HT & RCT.

Reaction temp. [°C]	Power [W]	Heating time [min]	Reaction time [min]	Particle size [µm]
100	1000	5	5	2.38
110	1000	5	5	4.0
120	1000	5	5	0.97
130	1000	5	5	1.06
140	1000	5	5	0.97

Influence of parameter optimization during FAHM synthesis on carbon particle size

The parameters during microwave assisted FAHM synthesis like reaction temperature (RT), heating time (HT) and reaction time (RCT) as well as subsequent temperature of pyrolysis step (T_{Py}) were optimized with respect to particle size (see Figure 2) as well as graphitization level, respectively.

First, reaction temperature variation was carried out while keeping power (P), heating time (HT), reaction time (RCT) and T_{Py} constant as 1000 W, 5 min, 5 min and 900 °C, respectively (Table 1). At reaction temperatures of 100 and 110 °C, well-defined particles of 2.4 and 4.0 µm were yielded, respectively as can be seen from SEM images in Figure 2a. The degree of sphericity was higher when microwaves were used.[63] Interestingly, synthesis at 120 °C led to formation of well-defined particles with a lower mean diameter in the range of 0.97 µm, whereas synthesis at 140 °C resulted in numerous particles with undefined shape. Therefore, 120 °C was considered as optimal value for RT and chosen for the next parameter variations. Study of Tao et al.[64] showed decrease in particle size from 737.7, 687.1 and 615.1 nm with increase in reaction temperatures at 20, 30 and 40 °C, respectively.

Since nucleation of polymer particles is expected to start during the heating time, influence of HT on particle size was investigated while keeping RT, RCT and P constant. From the SEM images shown in Figure 2b, it appears that heating time of 5 min has produced smallest (0.97 µm) and better particle size distribution compared to other experiments. Surprisingly, syn-

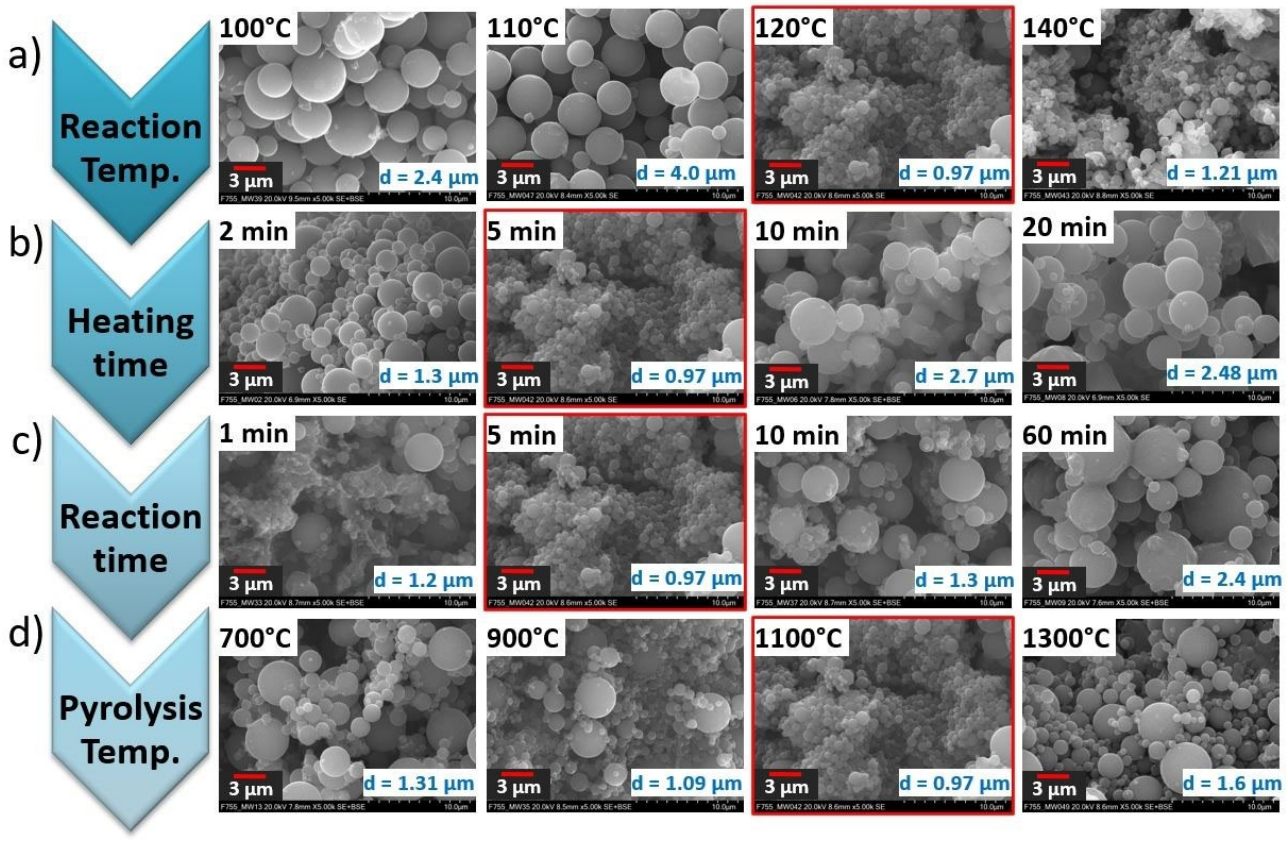

Figure 2. SEM images of C_{FAHM} from 17 M solution at different a) reaction temperature, b) heating time, c) reaction time and d) pyrolysis temperature. Average particle size "d" of each carbon is given in the respective images.

thesis with 2 min heating time delivered larger particles (1.3 µm) than that of 5 min (in Table 2). In this short hating period, however, microwave system was able to reach only 80 °C. Longer HT allowed further nucleation resulting in large (> 2 µm) carbon particles and wide particle size distribution where too long heating time obviously affects particle shape. In order to further reduce the mean particle size below 1 µm, variation of reaction time was explored. Experiments with shorter reaction times were expected to produce smaller and homogeneous particle morphology. However, reaction time of 1 and 2.5 min led to incomplete nucleation step (Figure 2c). As expected, longer reaction time of 7.5 and 10 min generates particle with larger diameter of 1.34 and 1.69 µm (in Table 3). Further longer reaction time of 60 min partially affected the particle shape along with bigger particle size of 2.3 µm, respectively (Figure S2). 5 min was proven to be optimal reaction duration that led to the smallest particle diameter of 0.97 µm and good homogeneous particle distribution throughout the sample. The trend is in good agreement with Arif et al.[62] study, in which, however, much smaller particles were collected. The particle size in their study dropped from 175 nm

Table 2. Influence of heating time on carbon particle size at constant P, RCT & RT.

Heating time [min]	Power [W]	Reaction temp. [°C]	Reaction time [min]	Particle size [µm]
2	1000	80	5	1.3
5	1000	120	5	0.97
10	1000	120	5	2.7
20	1000	120	5	2.48

Table 3. Influence of reaction time on carbon particle size at constant P, HT & RCT.

Reaction time [min]	Heating time [min]	Power [W]	Reaction temp. [°C]	Particle size [µm]
1	5	1000	120	1
2.5	5	1000	120	1
5	5	1000	120	0.95
7.5	5	1000	120	1.5
10	5	1000	120	1.5
60	5	1000	120	2.5

to 155 nm for reaction time of 1 and 5 min, since polystyrene latex was used as the template. Lower reaction times via microwave were studied by Chen et al.[59] where they synthesized cobalt carbon cubes at reaction RCT of 1.5 min. Liu et al.[65] found an optimum RCT at 10 min for their porous carbon synthesis by using lower power of 100 W. From Figure 2d, it can be observed that pyrolysis temperature T_{Py} influence C_{FAHM} particle size as well. The polymer synthesized at RT of 120 °C, HT of 5 min, RCT of 5 min was used for the T_{Py} study. Interestingly, increase in pyrolysis temperature T_{Py} from 700 up to 1100 °C resulted in a reduction in particle size in the range of 1.31 and 0.75 μm, respectively. At T_{Py} = 1300 °C, however, a mean particle size of 1.56 μm has been measured. During the pyrolysis, the shrinkage effect occurring can be explained by the by the loss of formaldehyde and the framework containing water.[65] The increase in particle size at 1300 °C can be explained by decrease in N-content since N atom helps to avoid the agglomeration of the particles. The reduction of pore size and pore volume while increasing the T_{Py} from 800 to 1200 °C was reported in earlier works.[29]

By comparing SEM images of C_{FAH} (Figure 1b) with those of C_{FAHM} (Figure 2d), it is obvious that both microwave effect and increase of pyrolysis temperature led to relatively lower particle size. FAH method resulted in carbon particles with wider particle size distribution (1–10 μm) and larger particle shape than those produced via microwave-assisted route that enables shorter reaction time (5 min vs. 12 h) by keeping identical reaction temperature of 120 °C. Thus, optimal particle size distribution of 5 and 0.75 μm was yielded at T_{Py} = 900 and 1100 °C for C_{FAH} and C_{FAHM} samples, respectively.

Influence of pyrolysis temperature on graphitization level of carbon samples

Influence of pyrolysis temperature T_{Py} on the C_{FAH} and C_{FAHM} structure was examined by XRD technique and compared to that of commercial graphite (KS6L) and carbon black and (VulcanXC-72R) samples. In spectra of C_{FAH} (Figure 3a) and C_{FAHM} (Figure 3b) samples pyrolyzed at 700, 900, 1100 and 1300 °C, two well-pronounced peaks were observed at $2\theta = 24–25°$ and $2\theta = 43–44°$ corresponding to the (002) plane of graphitic carbon and (100) plane of amorphous carbon respectively.[67] All the samples showed broad peaks, indicating predominance of amorphous domains that is confirmed in Liu et al. report.[67] In Figure 3c, the patterns of C_{FAH} and C_{FAHM} samples pyrolyzed at 900 °C is compared with those of commercially available KS6 L graphite and Vulcan carbon materials. KS6 L which has high degree of graphitization (91.7 %)[65] exhibited an intense narrow peak at $2\theta = 26.55°$. whereas, Vulcan which is turbostratic, (mixed graphitic and amorphous domains) exhibited a wide peak at $2\theta = 24.85°$. The shape of C_{FAH} and C_{FAHM} peaks is more similar to that of Vulcan. The amorphous nature and increase in structural defects for N-doped carbon obtained with similar precursors was observed by Kan et al.[70] and XRD pattern of carbon spheres synthesized by Banham et al.[17] exhibited similar landscape as well. In Chen et al.[58] study, all types of the hollow

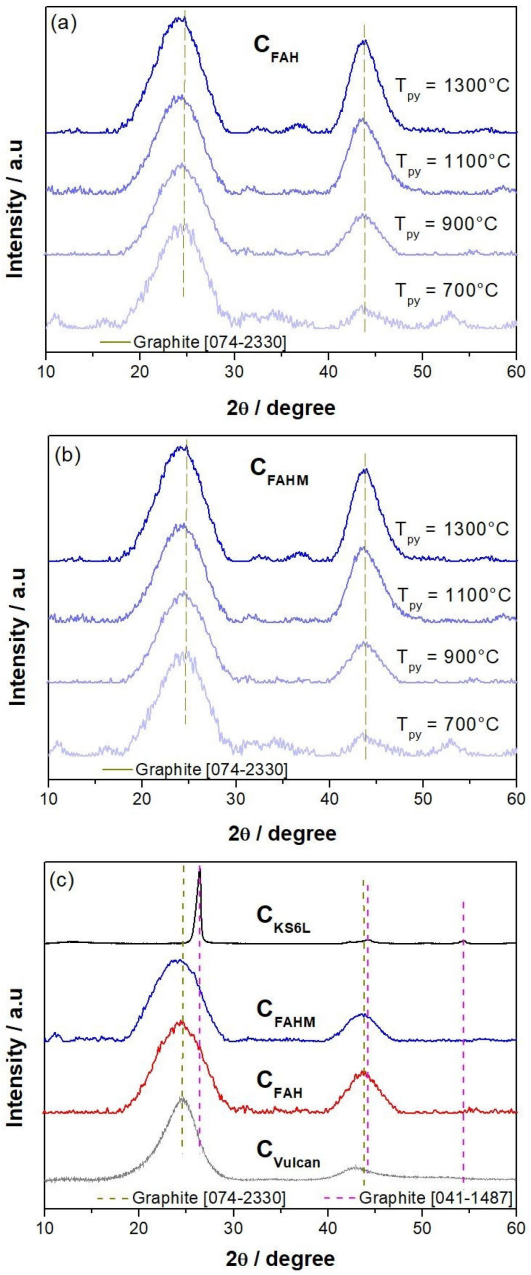

Figure 3. XRD patterns of a) C_{FAH} and b) C_{FAHM} at T_{Py} between 700–1300 °C and c) of both systems at T_{Py} = 900 °C compared to carbon black C_{Vulcan} and graphitic carbon C_{KS6L}.

carbon cubes synthesized by thermal reduction showed clear peaks at about 23.9° and 43.5° corresponding, to the (002) and (100) diffraction planes of graphite, respectively. Notably, the peak intensity at $2\theta = 44°$ for C_{FAH} and C_{FAHM} samples rises with higher T_{Py} values indicating increase in structural defects and disorder.[45] Among as-prepared carbons in this work, amount of graphitic domains culminates for samples pyrolyzed at 1300 °C. A close observation of all the peaks at $2\theta = 24.8°$ clearly shows a slight shift of the peak maximum towards lower angle values with increase of T_{Py}, that can be an indication for an increase in graphitization level.[71]

Influence of pyrolysis temperature on Raman spectra of C_{FAH} and C_{FAHM} presented in Figure 4 a–b is obvious that are characterized by two remarkable peaks related to graphitic lattice G band ($1595 \pm 5\ cm^{-1}$) and the defect-related D band ($1350 \pm 5\ cm^{-1}$). Independently on synthesis route, it can be seen that intensity of the D band increases significantly with higher pyrolysis temperature values. This increase in defects with increase in T_{py} is in good agreement with the XRD results. The polymer spheres contain functional groups which are partially lost during pyrolysis giving rise to graphitic and defect domains. The intensity ratio of D band to G band (I_D/I_G) provides qualitative information about the graphitic degree in carbon materials. The I_D/I_G values for C_{FAH} at T_{Py} in the range of 700–1300 °C are found to be 0.605, 0.614, 0.768 and 0.803 respectively. Similarly, for the same range of T_{Py}, C_{FAHM} exhibited I_D/I_G values 0.418, 0.434, 0.695, 0.713, respectively for T_{Py} 700–1300 °C. The higher I_D/I_G values indicate higher structural defects or amorphous carbon ratio within carbon material structure.[72] The above results are in good agreement with the study conducted by Bayatsarmadi et al.[66] in which I_D/I_G values also increased as T_{Py} was elevated from 700 to 1000 °C. This comparison shows that the pyrolyzed samples contains predominant defective domains at higher T_{Py}, which can be advantageous for catalyst support application. The increase in defects generates more available surface area helping to better dispersion of nano-catalyst that might favour charge transfer in adsorption process.[73] Jia et al.[74] claim that defect caused by the removal of N from carbon surface during pyrolysis step can enhance catalytic activity. The effect of T_{Py} on N content is discussed later. Similarly, Zhang et al.[75] measured Raman spectra of graphitic oxide and explained that the peak at ca. 1335 and 1590 cm^{-1} for D and G band, respectively indicates the structural defect and graphitic nature respectively. In Figure 4c, Raman spectra of C_{FAH} (T_{Py} = 900 °C) and C_{FAHM} (T_{Py} = 1100 °C) samples are compared to those of KS6 L and Vulcan XC-72R. The relevant information about peak position and calculated peak intensity ratios are summarized in Table 4. A clear sharp peak. related to second-order 2D band reflex is observed in the Raman spectra of KS6L graphite compared to the broader band of other materials that comparatively confirms low graphitization level of as-synthesized carbons and Vulcan sample. The thermal stability of the as-prepared carbons obtained from FAH and FAHM routes was investigated under oxidative atmosphere using thermogravimetric analysis (TGA) and compared with that of commercial C_{Vulcan} and C_{KS6L} samples (see Figure 5). It appears that increase of pyrolysis temperature up to 1300 °C clearly enhance thermal stability of both C_{FAH} and C_{FAHM} samples. First weight loss observed below 100 °C in both C_{FAH} (Figure 5a) and C_{FAHM} (Figure 5b) plots is due to evaporation of residual moisture. By closer examination of profiles, it can be noted that carbon pyrolyzed at 700 °C had higher moisture content than 1300 °C sample. No further substantial weight loss occurs until 300 °C in both cases. In the temperature range of 500–1100 °C, however, a substantial and similar mass loss is observed for both as-prepared carbon samples that is induced

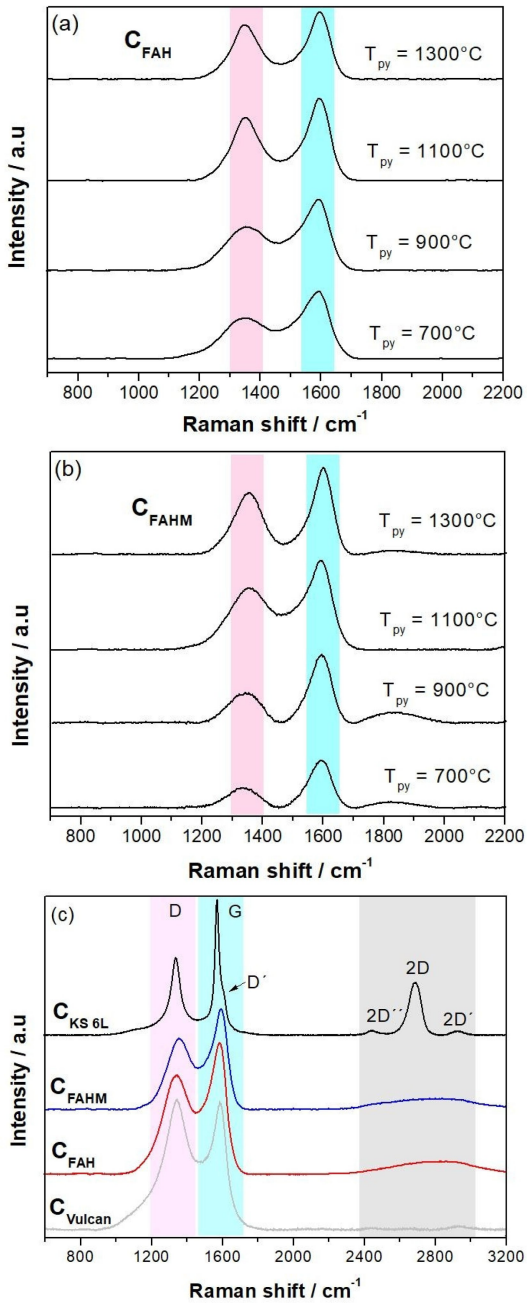

Figure 4. Raman spectra of a) C_{FAH} b) C_{FAHM} at different T_{Py} between 700–1300 °C and c) both systems compared to C_{Vulcan} and C_{KS6L}.

Table 4. Summary of some relevant information from Raman spectra of as-prepared C_{FAH} and C_{FAHM} carbons compared to those of KS6 L and Vulcan XC-72R reference samples.

Carbon	Band	Peak position [cm^{-1}]	I_D/I_G
C_{FAH} (T_{Py} = 900 °C)	D	1351.1	0.614
	G	1594.7	
C_{FAHM} (T_{Py} = 1100 °C)	D	1351.1	0.695
	G	1594.7	
KS6 L	D	1344.2	0.575
	G	1578.6	
Vulcan XC-72 R	D	1350.1	1.196
	G	1584.4	

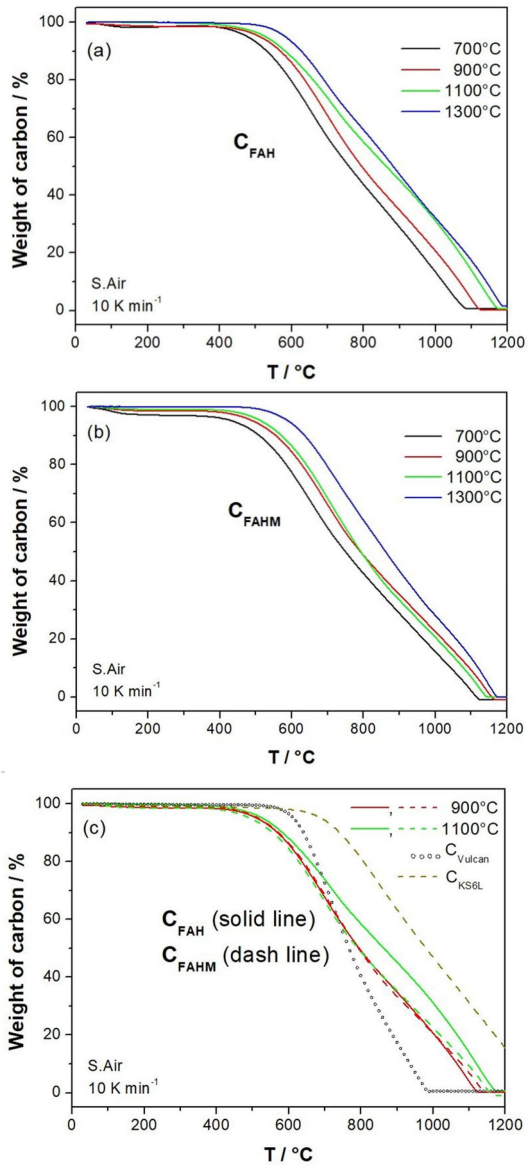

Figure 5. TGA profile of normalized weight retention of different (a) C_{FAH} (b) C_{FAHM} and c) both systems compared to C_{Vulcan} and C_{KS6L}.

by carbon burning in oxidative atmosphere. It can be noted that thermal stability of C_{FAH} and C_{KS6L} (Figure 5b) that can be explained by predominance of graphitic domains in synthetic graphite sample. This behavior of N-doped carbon suggests that the thermal stability of N-doped carbon increases with an increase in T_{Py}.

Effect of swelling agent

The effect of xylene additive during polymer synthesis on the carbon particle size and pore size distribution of C_{FAH} and C_{FAHM} can be observed in SEM images shown in Figure 6a. While C_{FAH} (T_{Py} = 900 °C) and C_{FAHM} (T_{Py} = 1100 °C) showed spherical particle shape, xylene-swelled $C_{FAH\text{-}xy}$ (T_{Py} = 1100 °C) showed some distortion in morphology. Some of the particles showed a rod-like shape (S4) that can be ascribed to irregular swelling of the template.[37] In contrast, xylene-swelled $C_{FAHM\text{-}xy}$ (T_{Py} = 1100 °C) retained its spherical shape completely. T_{Py} values were chosen based on the conductivity of the carbon (Table 6). Since xylene is hydrophobic and reacts with its counterpart of PO chain in F127 ($PEO_{106}PPO_{70}PEO_{106}$), the reaction rate is usually limited. Very long reaction time of 12 h for $C_{FAH\text{-}xy}$ synthesis appears to be reason for slight particles distortion. The average particle size of $C_{FAH\text{-}xy}$ and $C_{FAHM\text{-}xy}$ was 2.36 and 1.03 μm, respectively.

During physisorption experiment, C_{FAH}, $C_{FAH\text{-}xy}$, C_{FAHM}, and $C_{FAHM\text{-}xy}$ carbon samples exhibit type-IV hysteresis which is an indication for mesoporous domains (see Figure 6 and isotherms of C_{FAH} and $C_{FAH\text{-}xy}$ in S5). The cumulative (both micro/mesoporous) surface area and pore width was calculated using BET and DFT while mesoporous contribution alone was evaluated by Barrett-Joyner-Halenda (BJH) method. As can been observed from the values listed in Table 5, effect of swelling agent on pore surface area is significant only during hydrothermal polymer synthesis. Based on the DFT calculations, $C_{FAH\text{-}xy}$ exhibited a higher surface area of 113.36 $m^2 g^{-1}$ that represent nearby a factor 20 and a higher pore volume of 0.109 $cm^3 g^{-1}$ (Table 5) that logically led to an increase in bulk volume (Figure 7) compared to material without swelling agent. This might be due to a complete solubilization or micro emulsification[33] reaction of xylene with PO chains due to a long reaction time of 12 hour during FAH route.

The low mesopore voids is often observed when F127 is used as surfactant. The swelling corresponds to the hydrophobic PPO domains of the F127 (PEO_{106}-PPO_{70}-PEO_{106}) micelles with which the hydrophobic xylene reacts.[37] Since the PPO domains are limited to 30% of F127, the xylene intake is limited and thus the swelling effect of swelling agent during microwave-assisted synthesis is inexistent. Moreover, a decrease of about 18% in DFT pore surface was measured that can be

Table 5. Physical properties of carbon samples.

Carbon system	S_{BJH}[a] [$m^2 g^{-1}$]	S_{DFT}[b] [$m^2 g^{-1}$]	S_{BET}[b] [m^2/g]	Pore width[b] [nm]	Pore width[a] [nm]	Pore Volume[b] [$cm^3 g^{-1}$]	Bulk Volume [$cm^3 g^{-1}$]
C_{FAH}	3.45	5.86	5.34	1.43	3.54	0.008	1.29
$C_{FAH\text{-}xy}$	56.67	113.36	124.16	0.93	3.44	0.109	2.11
C_{FAHM}	24.19	38.27	39.76	0.85	3.02	0.051	1.58
$C_{FAHM\text{-}xy}$	18.47	31.49	33.87	0.93	2.95	0.058	1.62
C_{Vulcan}	–	234.87	235.56	0.93	–	0.311	12.61

[a] mesoporous. [b] micropores & mesopores, S-Surface area

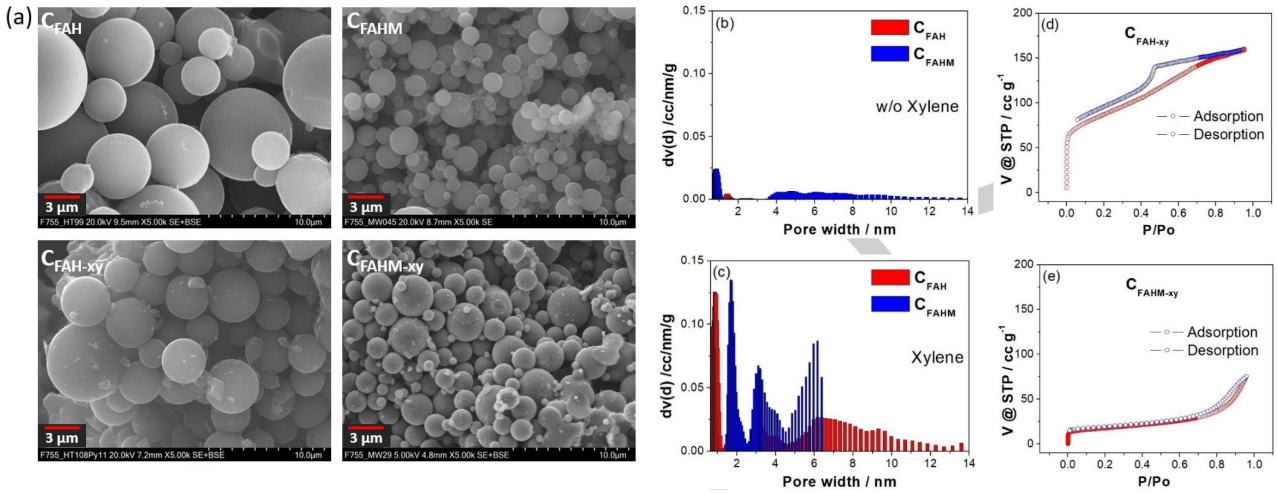

Figure 6. a) SEM images (top row), b&c) pore width distribution and d&e) corresponding isotherms of $C_{FAH\text{-}xy}$ (T_{Py} = 1100 °C) and $C_{FAHM\text{-}xy}$ (T_{Py} = 1100 °C) with xylene.

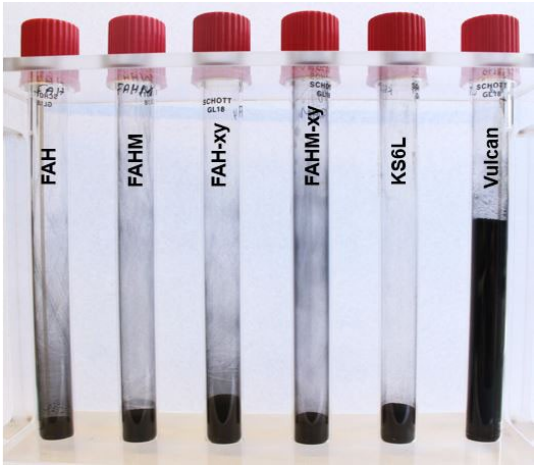

Figure 7. Bulk volume of 1 g of different carbon samples.

explained by too short reaction time. Nevertheless, it should be noted that DFT specific area of 38.3 $cm^2 g^{-1}$ calculated for C_{FAHM} is about 6.5 times higher than that of C_{FAH} material.

The decrease in mean pore size width from DFT method of 1.43 down to 0.93 nm for C_{FAH} material can be obviously attributed to more pronounced increase in microporous domains. Interestingly, pore mean width of mesopores remains nearly unchanged in the range between 2.95 and 3.54 nm for both carbon samples, whereas the pore volume increased in $C_{FAH\text{-}xy}$ from 0.008 to 0.109 $cm^3 g^{-1}$. From the pure aspect of carbon sample functionality as Pt catalyst support, high volume of mesopores is desired. The Raman spectra and I_D/I_G values are added to the supplementary document as S6.

Influence of pyrolysis temperature on carbon conductivity

As expected, electronic conductivity (Eq. 1) of C_{FAH} and C_{FAHM} samples soared with increasing in T_{Py} where highest value of 8.65 S cm^{-1} was yielded after 1300 °C treatment of C_{FAH}. The resistivity and resistance of carbon materials was derived from the equation 2 & 3, respectively. Interestingly a 10-fold improvement of conductivity was, observed when T_{Py} was raised from 700 to 900 °C that is assigned to increase in graphitization level as already mentioned in Raman spectra (in above section). Surprisingly, maximal conductivity of C_{FAHM} samples amounts to 6.2 S cm^{-1} after 1300 °C treatment. The about 17% lower value compared to that obtained by FAH route might be explained by the particle size distribution. Sircar et al.[76] showed that with wider particle size distribution, the conductivity can increase. For C_{FAH} carbon, the particle size distribution ranged from 1–10 µm, whereas in C_{FAHM} carbon it was from 0.75–4 µm. The average particle size of C_{FAH} samples was about 4.6 µm and mean particle size of C_{FAHM} was in the range of 1 µm or lower. All the values are available in Table 1. The rise of conductivity with increased T_{Py} is in good agreement with the work of Datta et al.[39] in which increase from 2.5 S cm^{-1} at T_{Py} = 800 °C up to 80 S cm^{-1} at 1000 °C. is mentioned. In Figure 8b, carbons synthetized with swelling agent show the same tendency, whereas conductivity values are lower (Table 6) compared to the carbons without swelling agent. This is due to core region

Table 6. Influence of T_{Py} on electronic conductivity of as-prepared carbon samples.

Pyrolysis Temp. [°C]	C_{FAH} σ [S cm^{-1}]	C_{FAHM} σ [S cm^{-1}]	$C_{FAH\text{-}xy}$ σ [S cm^{-1}]	$C_{FAHM\text{-}xy}$ σ [S cm^{-1}]
700	0.656	0.735	0.23	0.75
900	5.604	2.828	2.26	1.81
1100	8.541	5.643	3.83	5.01
1300	8.648	6.239	3.86	5.89

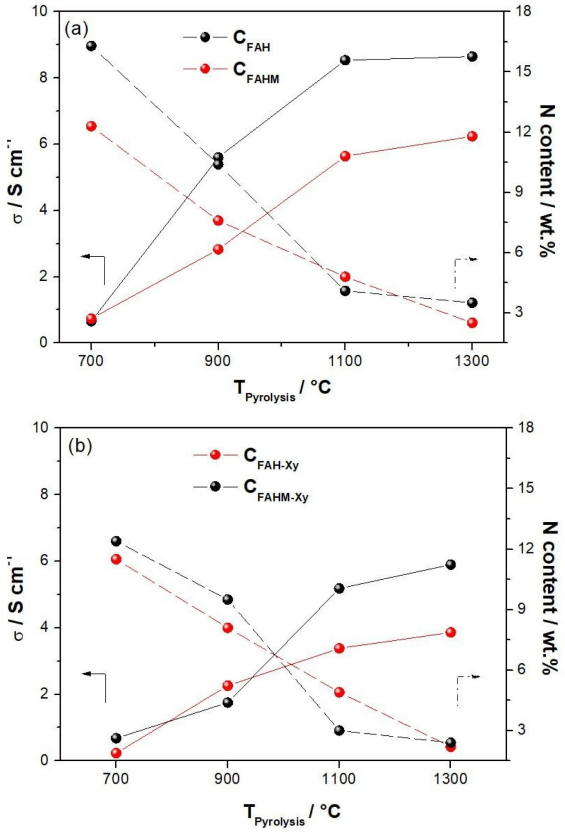

Figure 8. Conductivity plot and N-content of a) C_{FAH} and C_{FAHM} at T_{Py} and b) C_{FAH-xy} and $C_{FAHM-xy}$ between 700 and 1300 °C.

swelling, occurring from xylene interacting with hydrophobic PPO chains. Conductivity values of KS6L & C_{Vulcan} samples amounts 10.23 and 3.8 S cm^{-1}, respectively.

Evaluation of N content in carbon by EDAX, CHN and XPS analysis

The amount of nitrogen present in C_{FAH}, C_{FAHM}, C_{FAH-xy} and $C_{FAHM-xy}$ carbon was determined by EDX and CHN analysis while nature of nitrogen species was examined by XPS analysis. Because of limited experimental resources, however, XPS survey was conducted only for some selected C_{FAH}, C_{FAHM}, C_{FAH-xy} and $C_{FAHM-xy}$ samples with electronic conductivity as most relevant criteria for selection (Table 7). From EDX study (Figure S7), a clear decrease in N content with increasing T_{Py} from 900 to 1100 °C is obvious that amounts to 27.5, 40, 34 and 28 % in case of C_{FAH}, C_{FAHM}, C_{FAH-xy} and $C_{FAHM-xy}$, respectively according to CHN analysis. This is in good accordance with 30 % N loss reported by Yang et al.[76] within T_{Py} 800 to 1000 °C temperature range. Highest N concentration values in the range of 6.3–7.1 wt% were measured for samples pyrolyzed at 700 °C. Furthermore, EDX measurement revealed that C_{FAH} and C_{FAHM} contain less than 0.03 % of sulfur compared to 1 wt% in carbon Vulcan. The presence of ca. 5000 ppm or higher concentration was found to be potentially poisonous to the fuel cells.[77] As can be seen in Table 7, N concentration in carbon samples obtained from CHN analysis follows the same trend as those measured by EDX technique, whereas absolute values differ substantially. The XPS deconvolution was done to investigate chemical state of doped N 1s and C 1s in selected highly conductive samples C_{FAH} (T_{Py} = 900 °C, 5.6 S cm^{-1}), C_{FAHM} at (T_{Py} = 1100 °C, 5.64 S cm^{-1}), C_{FAH-xy} (T_{Py} = 1100 °C, 3.83 S cm^{-1}) and $C_{FAHM-xy}$ (T_{Py} = 1100 °C, 5.01 S cm^{-1}). The respective N content is available in Table 7. From the deconvoluted N 1s spectra exhibited in Figure 9, four types of nitrogen groups were identified. The contribution of N pyrrolic to overall N 1s signal prevails in all the carbon samples. At 398.5 eV, pyridinic state of the nitrogen atom forms one sigma-bond with one neighboring carbon atom as well as one sigma and one pi-bond with the other neighboring nitrogen atom.[79] These neighboring carbon atoms with Lewis basicity play an important role as active sites for oxygen molecule adsorption during the initial step of the ORR.[77] The peaks at 401.3 and 403.5 eV address the pyrrolic and graphitic sp3-

Table 7. Summary of particle size, conductivity and N-content of all the carbon samples for different pyrolysis temperatures.

System	T_{Py} [°C]	Size [μm]	σ [S cm^{-1}]	N (EDX) [wt %]	N (CHN) [wt %]	N (XPS) [wt %]
C_{FAH}	700	4.58	0.66	15.5	6.79	–
	900	5.03	5.60	9.5	4.92	3.9
	1100	5.09	8.54	4.9	1.61	–
	1300	4.26	8.65	3.4	0.91	–
C_{FAHM}	700	1.31	0.74	11.8	7.11	–
	900	1.09	2.83	7.4	4.28	2.1
	1100	0.75	5.64	4.6	1.95	1.7
	1300	1.56	6.24	2.3	0.83	–
C_{FAH-xy}	700	2.13	0.23	11.79	6.6	–
	900	2.36	2.26	9.01	4.03	–
	1100	3.1	3.83	2.48	1.79	1.6
	1300	3.26	3.86	2.44	0.93	–
$C_{FAHM-xy}$	700	2.23	0.75	11.21	6.3	–
	900	1.03	1.81	6.96	3.92	3.6
	1100	0.99	5.01	4.83	1.9	1.9
	1300	1.3	5.89	2.96	0.95	–

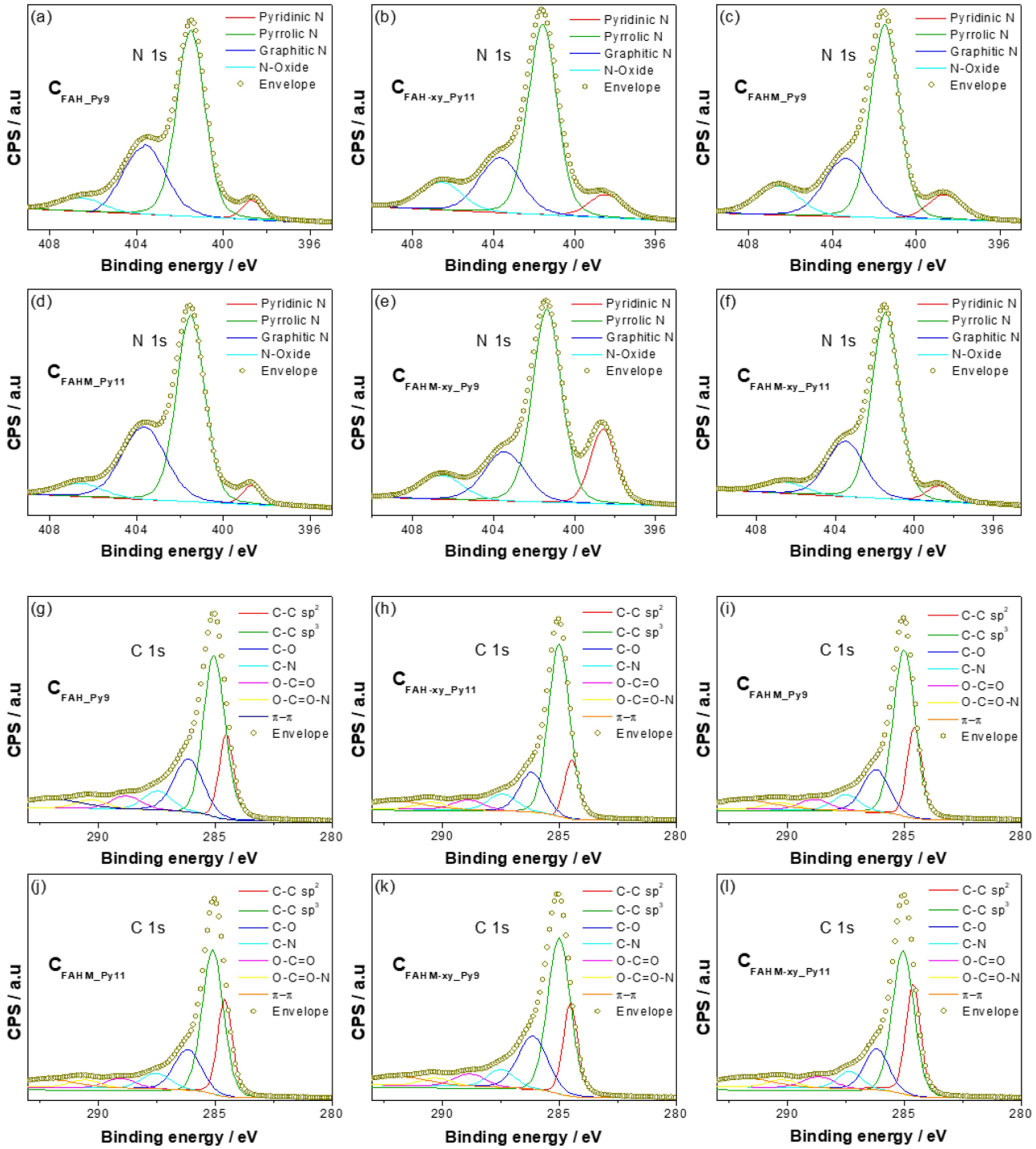

Figure 9. XPS spectra and respective peak deconvolution relative to binding energy of nitrogen 1 s (a, b, c, d, e, f) from core level C_{FAH}, C_{FAHM}, $C_{FAH\text{-}xyPy9}$, $C_{FAH\text{-}xyPy11}$, $C_{FAHMxyPy9}$ and $C_{FAHMxyPy11}$ surface respectively.

hybridized nitrogen state, respectively. The graphitic peak is induced by the presence of a (–C–N=N–C–) arrangement (Figure 9).[29] The shape of the N 1s signal is obviously depending on pyrolysis temperature T_{Py}. At higher temperatures than 800 °C, pyridinic N can be converted into graphitic N, that exhibits high activity towards ORR.[63]

In Figure 9 c–d, increase in graphitic N and decrease in N-Oxide can be observed when the T_{Py} raises from 900 to 1100 °C in C_{FAH} and C_{FAHM}. This behavior is confirmed elsewhere.[67] The same trend is observed for xylene-swelled carbon (Figure 9e–f). The pyrrolic N decreased implying the instability of those species at. higher temperatures.[81] The final peak at 406 eV is ascribed to the N- Oxide with a small fraction of NO_3^-/NO_2

Research Article
doi.org/10.1002/cctc.202201556
Chemistry Europe
European Chemical Societies Publishing

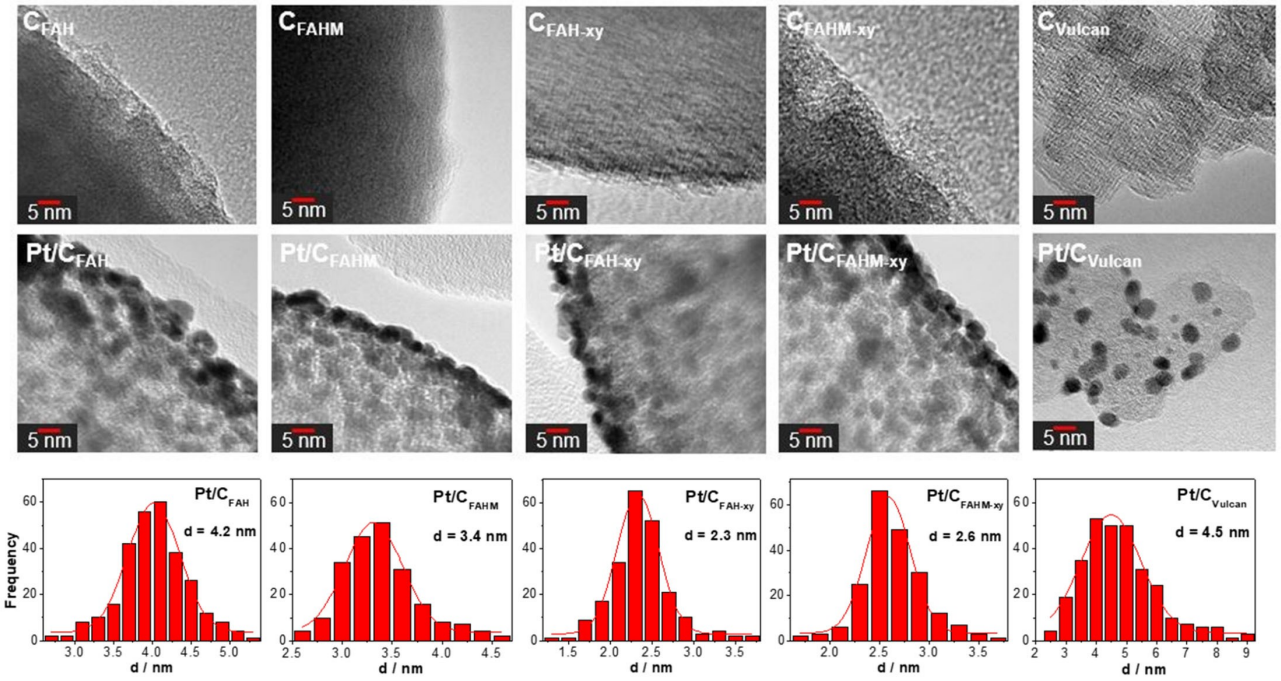

Figure 10. TEM images of different carbons and Pt particles on C_{FAH}, C_{FAHM}, $C_{FAH\text{-}xy}$, $C_{FAHM\text{-}xy}$ and C_{Vulcan} with corresponding Pt particle size distribution histograms.

groups.[29] The total N amount in selected samples of each species is mentioned in Table 7. Every deconvoluted high-resolution C 1s spectrum displayed in Figure 9b consists of seven peaks. The C 1s signals are centred predominantly at 284.5 and 285 eV which are assigned to sp^2 and sp^3 hybridized C–C bonds, respectively. These results are in good agreement with those reported by Gao et al.,[82] where N-doped carbon foams were pyrolyzed at 600 and 1200 °C. The increase in T_{Py} slightly shifted the C 1s to 285.2 eV in case of T_{Py} = 1100 °C. This shift is supported by XRD (Figure 4) and Raman studies (Figure 5). The other peaks centred at 286.15, 287.47, 288.83, 290.31 and 291.99 eV correspond to C–O, C–N, O– C=O, O=C–O–N and π-π groups, respectively. The concentration of all carbon and nitrogen species are given in Supporting Information (Table 1).

TEM images of Pt/C catalysts

Figure 10 shows TEM images of the different carbons before and after deposition of 40 wt% nano-dispersed Pt as well as corresponding particle size distribution histograms. The surface morphology of all carbons prepared by soft-template route clearly differs from that of commercial C_{Vulcan} which is smaller in diameter (~50 nm). While C_{FAH} and $C_{FAH\text{-}xy}$ samples have a quite smooth surface, microwave- synthesized samples appear to have a rougher surface (Figure S7). The average size of Pt particles deposited on C_{FAH}, $C_{FAH\text{-}xy}$, C_{FAHM}, and $C_{FAHM\text{-}xy}$ was calculated from PSD histogram, which is in the range of 4.2, 3.4, 2.3 and 2.6 nm respectively, compared to 4.5 nm for Pt/C_{Vulcan}. Surprisingly, Pt distribution on the as-synthesized carbon supports is more dense and not as homogeneous as on C_{Vulcan} surface.

Electrochemical characterization of Pt/C catalysts

a) Experiments with Pt/C powder on RRDE

The cyclic voltammograms (CVs) of all carbon-supported Pt samples displayed in Figure 11 show typical electrochemical behavior of H_{ads}/H_{des}, double layer capacitance and oxide formation/reduction regions. The double layer capacitance

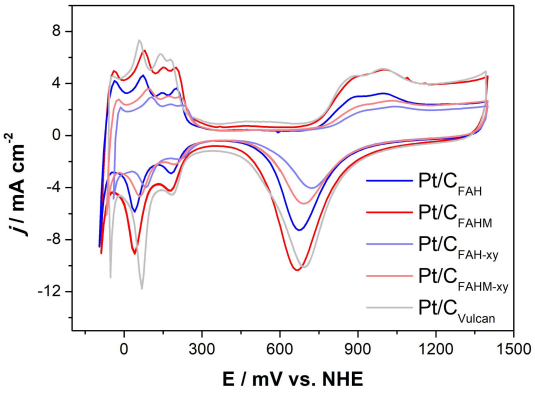

Figure 11. CV of different 40 wt% Pt/C (80 μg_{Pt} cm^{-2}) in N_2-saturated 0.5 M H_2SO_4 at 40 mV s^{-1} and 23 °C after 20 initial CVs.

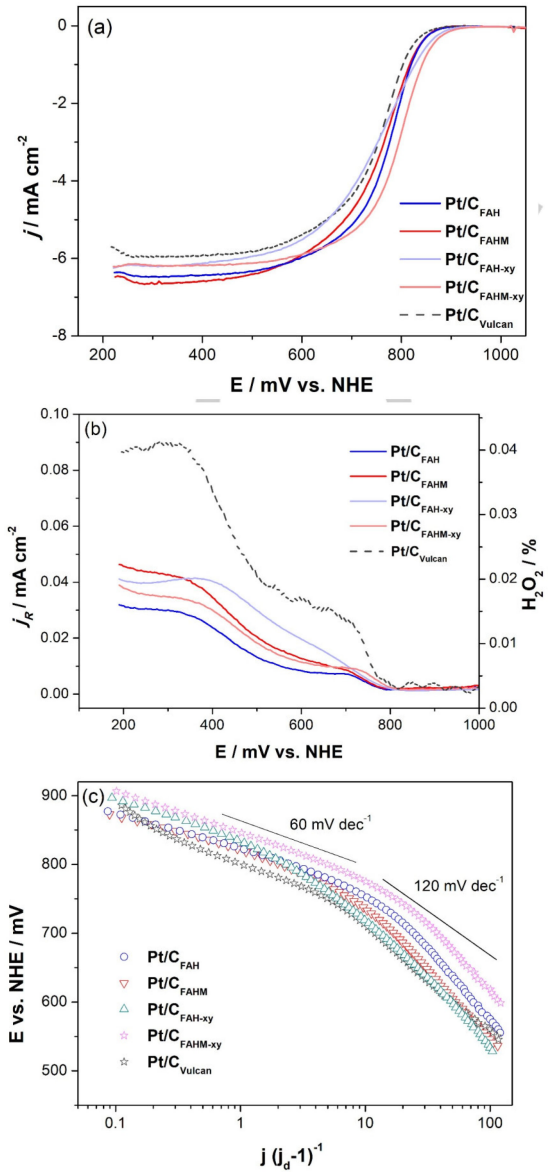

Figure 12. Polarization curves of different 40 wt% Pt/C in O_2-saturated0.5 M H_2SO_4 at 1600 rpm, 5 mV s^{-1} and 23 °C (a) GC disc, (b) Pt ring electrode at 1.2 V steady-state potential (collection efficiency = 0.23) and (c) Tafel slope from LSV measurements.

region in the case of Pt/C_{FAHM} is more pronounced than that measured for other systems including Pt/C_{Vulcan} reference. This effect can be attributed to the smallest particle size of Pt on C_{FAHM} (Table 5). The Pt electrochemically active surface area (ECSA) was evaluated by integrating hydrogen adsorption peak during cathodic scan. The ECSA values of Pt/C_{FAH} was 58.45 $m^2 g^{-1}$, whereas Pt/$C_{FAH\text{-}xy}$ and Pt/$C_{FAHM\text{-}xy}$ showed ECSA of 41.32 and 45.52 $m^2 g^{-1}$, respectively representing almost half the value of Vulcan (Table. 8). Pt/C_{FAHM} showed comparatively closer ECSA (81.26 $m^2 g^{-1}$) compared to carbon Vulcan (93.58 $m^2 g^{-1}$). This indicates high dispersion of Pt on Vulcan and comparable dispersion on Pt/C_{FAHM} due to the availability of more mesoporous region. Pt/C_{FAHM} had the Pt particles of size 3.4 nm and Pt/C_{Vulcan} had values of 4.5 nm (see Figure 10). Additionally, similar onset potential values are observed for Pt-OH formation at Pt/C_{Vulcan} and Pt/C_{FAHM} whereas, for other systems it started at lower potential. The difference in charge within hydrogen regions in case of the all the systems shows high discrepancy in catalyst accessibility despite identical mass loading.[18] Figure 12 illustrates the activity of the four as-prepared carbon supported Pt catalysts for (a) the oxygen reduction reaction (ORR) at the disc electrode and (b) H_2O_2 production (2 e^- reduction step) at the Pt ring electrode in comparison with that of Pt/C_{Vulcan}. In kinetic region all systems showed similar behaviour. In mixed diffusion/kinetic-controlled region (0.7-0.8 V), Pt/$C_{FAH\text{-}xy}$ and Pt/C_{Vulcan} showed higher over-potential of 14 mV at 2.5 mA cm^{-2} compared to that of Pt/$C_{FAHM\text{-}xy}$ sample. In diffusion- controlled regime, the limiting current density of all Pt/C samples was higher than the theoretical value of 5.3 mA cm^{-2} calculated for ORR in 0.5 M H_2SO_4 with reference to a 5 mm smooth geometrical electrode area of e. g. glassy carbon (A_{geo}) at 1600 rpm.[83] The higher limiting values yielded in that work might be assigned to the higher electrode surface area of the active catalyst layer (A_{rea}) compare to that of the electrode substrate (A_{geo}) as suggested by Shinde et al.[84] and calculated by Wang et al.[85] for different A_{rea}/A_{geo} ratios.

The mass and specific activity values of the carb on-supported catalysts listed in Table 8 were calculated by normalizing the geometrical current density at 0.8 V towards Pt loading and ECSA values, respectively. As observed in ORR, the Pt/$C_{FAHM\text{-}xy}$ showed the best mass activity and specific activity among the investigated Pt/C systems followed by Pt/$C_{FAH\text{-}xy}$. This higher activity arises from particle size, N-doping[29] and increased surface area. Guo et al.[80] reported that pyridinic N

Table 8. Summary of RRDE experiment results.

System	Pt $d_{avg.}$ [nm]	Tafel slope [mV dec^{-1}]	H_2O_2[c] [%]	ECSA[a] [$m^2 g^{-1}$]	Spec. activity[b] [mA cm^{-2}]	Mass activity[b] [mA mg_{Pt}^{-1}]	ECSA retention[d] [%]
Pt/C_{FAH}	4.2	60 - 120	0.015	58.45	0.0397	4.91	75
Pt/C_{FAHM}	3.4	60 - 120	0.021	81.26	0.0244	4.07	77
Pt/$C_{FAH\text{-}xy}$	2.3	60 - 125	0.019	41.32	0.2091	4.32	70
Pt/$C_{FAHM\text{-}xy}$	2.6	60 - 120	0.018	45.52	0.3105	7.06	79
Pt/C_{Vulcan}	4.5	60 - 127	0.040	93.58	0.0437	1.76	08

[a] ECSA calculated by integrating H_{ad} region in the CV between 0.005 and 0.36 V and the charge induced by a monolayer of hydrogen atoms on Pt amounts 210 μC cm^{-2}. [b] Specific and mass activity values are calculated for ORR @ 0.8 V, 1600 rpm. [c] The percentage of H_2O_2 estimated during ORR at 0.2 V, 1600 rpm. [d] ECSA retention in percent after 10,000 cycles stability test.

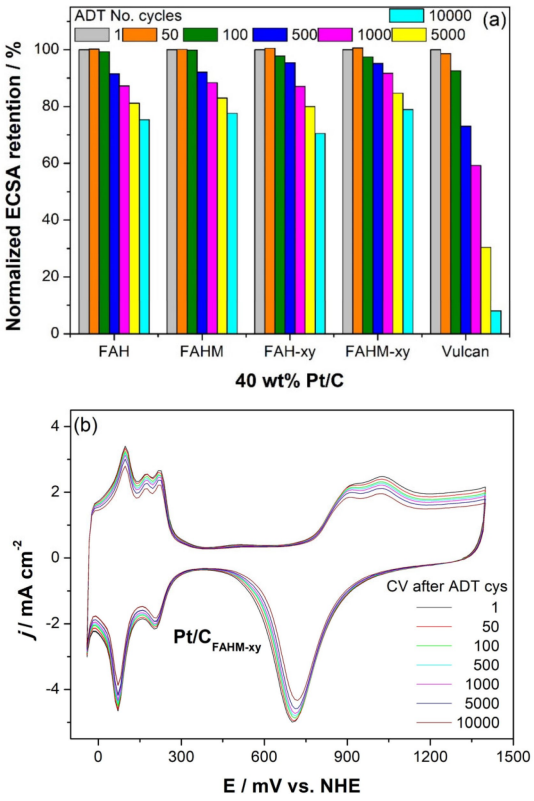

Figure 13. (a) Influence of ADT cycle number on ECSA retention of different GDEs in N_2 saturated 0.5 M H_2SO_4 at 1 $V s^{-1}$ and (b) CVs of 40 wt% $Pt/C_{FAHM-xy}$ (0.25 $mg_{Pt} cm^{-2}$) GDE at 40 $mV s^{-1}$ after a certain number of ADT cycles.

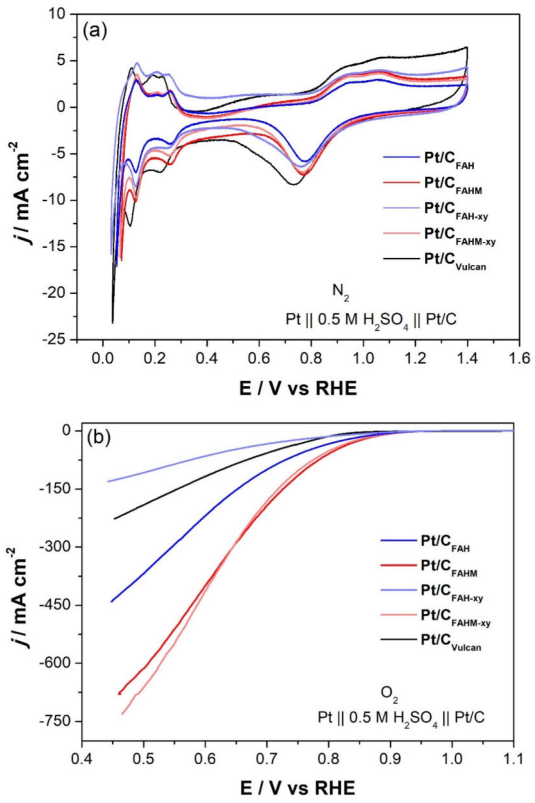

Figure 14. CV of GDEs in N_2 saturated 0.5 M H_2SO_4 at 40 $mV s^{-1}$ and (b) LSVs of different 40 wt% Pt/C GDEs (250 $\mu g_{Pt} cm^{-2}$) with 10 wt% Nafion and 20 wt % PTFE in O_2-saturated 0.5 M H_2SO_4 at 5 $mV s^{-1}$.

atom helps in creating active sites for ORR with well-defined π-conjugation. Moreover, these species can provide abundant -active sites by occupying edges or defect sites.[86] As suggested in our previous work,[29] this difference in overpotential can also be due to some disparities in surface activation, other functional groups, pore size distribution, accessibility of active sites as well as affinity to H_2O_2 formation. The amount of in-situ H_2O_2 production was estimated according to protocol in ref.[87] and the determined values listed in Table 8 are negligible. In Figure 12c, typical Tafel slope values of 60 and 120 $mV dec^{-1}$ were calculated for ORR activity at as-prepared Pt/C_{FAH}, Pt/C_{FAHM}, Pt/C_{FAH-xy} and $Pt/C_{FAHM-xy}$ catalysts in kinetics-controlled (850–750 mV) and mixed kinetics/diffusion-controlled (750–650 mV) domains (see Table 8). The corrosion tests of the Pt/C's in 1 M H_2SO_4 were carried out for 4 weeks and were tested using ICP-MS. The concentration of Pt for Pt/C_{FAH}, Pt/C_{FAHM}, Pt/C_{FAH-xy} and $Pt/C_{FAHM-xy}$ were 4.9, 4.2, 3.6 and 3.7 $\mu g L^{-1}$ respectively, compared to 160 $\mu g L^{-1}$ of Pt/C_{Vulcan}.

The transition region from low to high slope value that is situated at about 750–700 mV results from enrichment/depletion of the Pt surface hydroxide and oxide species on the catalyst surface (see CV in Figure 11). The ORR pathway and rate-determining step are supposed to be identical for all carbon supported Pt systems investigated. Figure 13a shows evolution of the ECSA-normalized retention of the different catalyst powders after as-mentioned number of ADT cycles on a glassy carbon electrode. ECSA loss during initial cycles arises from the dissolution of smaller Pt particles than 2 nm. Interestingly, ECSA retention of as-prepared Pt/C_{FAH}, Pt/C_{FAHM}, Pt/C_{FAH-xy} and $Pt/C_{FAHM-xy}$ catalysts after 10,000 ADT cycles are, 78, 77, 75 and 70%, respectively compared to the poor ECSA retention of 8% for Pt/C_{Vulcan}. Figure 13b illustrates the electrochemical response of the most stable $Pt/C_{FAHM-xy}$ system with increasing ADT cycles at a potential scanning rate of 40 $mV s^{-1}$. It is obvious that accelerated aging procedure affects some voltammogram regions mostly due to Platinum particle dissolution, migration and growth. is an indication for excellent

Table 9. Relevant ECSA retention values from RRDE and GDE experiments.

System	Pt/C_{FAH}		Pt/C_{FAHM}		Pt/C_{FAH-xy}		$Pt/C_{FAHM-xy}$		Pt/C_{Vulcan}	
ADT Cycles	RRDE	GDE	RRDE	GDE	RRDE	GDE	RRDE	GDE	RRDE	GDE
5,000	81%	76%	83%	84%	79%	73%	84%	85%	30%	27%
10,000	75%	70%	77%	73%	70%	65%	78%	80%	8%	13%

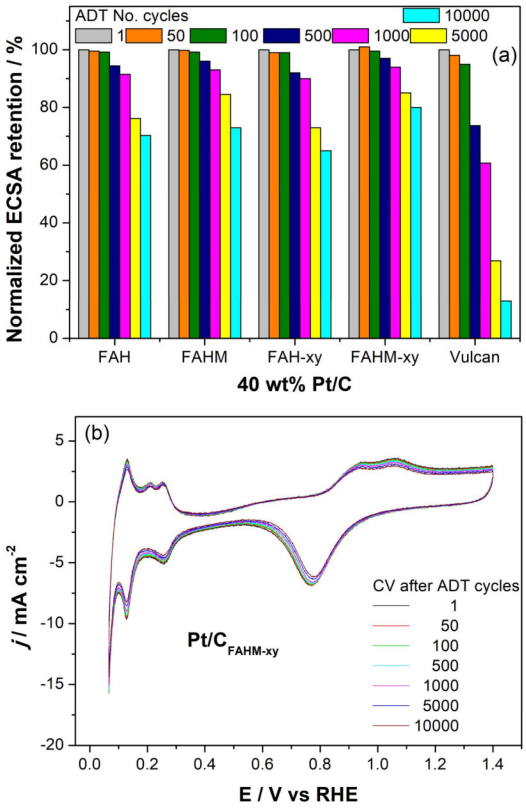

Figure 15. (a) Influence of ADT cycle number on ECSA retention of different GDEs in N_2 saturated 0.5 M H_2SO_4 at 1 V s^{-1} and (b) CVs of 40 wt% Pt/$C_{FAHM-xy}$ (0.25 mg_{Pt} cm^{-2}) GDE at 40 mV s^{-1} after a certain number of ADT cycles.

resistance of carbon support against oxidative corrosion process.

b) Experiments with Pt/C GDE

GDEs prepared with Pt/C_{FAH}, Pt/C_{FAHM}, Pt/C_{FAH-xy} and Pt/$C_{FAHM-xy}$ were tested electrochemically under half-cell conditions in absence and presence of molecular oxygen (Figure 14) and compared with Pt/C_{Vulcan} as reference. All GDEs were loaded with 250 μg_{Pt} cm^{-2} to keep the catalyst loading similar to state-of-the-art PEMFCs and were subjected to the same CV and ADT procedure under RRDE conditions. The activity of GDEs for ORR is of two orders of magnitude higher compared to the values obtained from RRDE. This is due to the higher oxygen concentration in the gas phase of the so- called three-phase boundary region compared to that in the liquid phase and is in good agreement with Henry's solubility (factor of 0.006).

Despite identical Pt loading, GDE with Pt/$C_{FAHM-xy}$ and Pt/C_{FAHM} clearly exhibited higher activity the ORR that reached 181 and 190 mA cm^{-2} at 0.7 V, respectively compared to 100 and 57 mA cm^{-2} for GDE with Pt/C_{FAH} and Pt/C_{Vulcan}, respectively (Figure 14b). In Figure 15a, ECSA retention of different GDEs as a function of ADT cycle number is shown. Analogous to the aging process with RRDE, GDE with Pt/$C_{FAHM-xy}$ catalyst showed the best corrosion resistance behavior with 80% ECSA retention 10,000 cycles followed by Pt/C_{FAHM} (73%), Pt/C_{FAH} (70%) and Pt/C_{FAH-xy} (65%), whereas for Pt/C_{Vulcan}, the value was only 13%. Also, here, double layer capacitance region of Pt/$C_{FAHM-xy}$ GDE remains stable during the complete procedure (Figure 15b) that confirms electrochemical stability of carbon support. Values listed in Table 9 reveal that ECSA retention values from GDE experiments well correlate well with those yielded from RRDE in which Pt/$C_{FAHM-xy}$ exhibits highest retention.

Conclusion

In this work, micro/mesoporous carbon spheres were successfully synthesized via conventional hydrothermal (C_{FAH}) route and microwave-assisted hydrothermal method (C_{FAHM}) by using Pluronic® F127 as a soft-template and m-Aminophenol as carbon source. The influence of the NH_4OH concentration and T_{Py} on the particle size was investigated in FAH method. The 17 M ammonia performed as the best catalyst concentration to give the best particle morphology. T_{Py} was not affected the particle size so much and particle size ranged from 4.3–5.5 μm.

Optimization of microwave-assisted FAHM synthesis regarding particle size resulted in heating time of 5 min, reaction time of 5 min at 120 °C reaction temperature for a given microwave power value of 1000 W. FAHM method helped to reduce the particle size as well as the reaction time, from 3 to 0.75 μm and 12 h to 5 min respectively, compared to non-microwave-assisted FAH method. As expected, jump of pyrolysis temperature T_{Py} from 700–1300 °C resulted in higher conductivity (87–94%) of both C_{FAH} and C_{FAHM} carbon samples caused by increase in both sp^3 and sp^2 hybridization, whereas N-content decreased (85–88%) along with increasing T_{Py} values. The electric conductivity of both C_{FAH} and C_{FAHM} measured in this work amounts to 5.6 and 5.64 S cm^{-1} respectively, well above that of that of C_{Vulcan} (3.8 S cm^{-1}) benchmark product. Respective pyrolysis temperature (T_{Py}) of corresponding polymers to reach the targeted conductivity was 900 and 1100 °C.

Xylene as a swelling agent was used to create more mesoporous domains that resulted in significant improvement of C_{FAH} pore volume from 0.008 to 0.109 $cm^3 g^{-1}$ while its BET surface area jumped from 5.8 up to 113 $m^2 g^{-1}$. By contrast, no increase was observed for C_{FAHM} samples that can be assigned to too short reaction time.

Xylene swelled Pt/C_{FAH-xy} and Pt/$C_{FAHM-xy}$ showed high specific activity and mass activity for ORR during RRDE experiments. All as-prepared carbon samples decorated with Pt showed low H_2O_2 production during the ORR in the RRDE compared to the Pt/C_{Vulcan} catalyst. Moreover, GDE with Pt/C_{FAH}, Pt/C_{FAHM}, Pt/C_{FAH-xy} and Pt/$C_{FAHM-xy}$ showed excellent ECSA retention of about 65–80% during accelerated degradation testing under half-cell conditions compared to only 13% for GDE with Pt/C_{Vulcan}. Although xylene-swelled C_{FAH-xy} had higher BET surface, microwave-synthesised $C_{FAHM-xy}$ carbon with smaller particle size of 0.75 μm appeared to be the best catalyst support.

Experimental Section

In this work, commercial carbon black (Vulcan XC-72R, Cabot) and graphitic carbon (KS6L, C-NERGY™ TIMCAL) were used as received for reference.

Carbon synthesis by F127- Aminophenol hydrothermal route (C_{FAH})

In a typical synthesis of polymer, 15 g of commercially available triblock amphiphilic copolymer Pluronic®-F127 (PEO_{106}-PPO_{70}-PEO_{106}) (Sigma-Aldrich, 99.25%) was dissolved in 180 ml of ultrapure distilled water (0.055 μS cm^{-1}, ELGA Millipore) by magnetic stirring at 600 rpm. Thereafter, 3.283 g of *m*-Aminophenol (MAP) (Alfa-Aesar, 98+%) and 2.1 g of hexamethylenetetramine (HMT) (Sigma-Aldrich, 99.9%) was added to the former solution and stirred at 600 rpm for 30 min. The pH of reaction solution was monitored with a glass electrode (Greisinger GmbH, GMH 5500 Series). The pH of the solution was adjusted to 10 by adding 30% aqueous ammonia solution (ROTIPURAN® 30%, p.a., ACS) drop wise to the solution. To find the optimum concentration of ammonia, a variation between 1 and 17 M was carried out. The mixture was stirred for another 30 min until a pale-yellow colour was obtained. The resultant reaction solution was transferred to a 250 ml Teflon lined autoclave and hydrothermally treated in the oven (BINDER, FD 23) at 120 °C for 12 h. This resulted in the formation of reddish-brown colored polymer. The mechanism of polymer formation can be seen in Scheme (The schematic diagram is provided in supplementary information as Scheme 1). For swelling agent studies, 7.5 ml of xylene was added to the solution after the addition of F127 template followed by the same procedure. The mass of xylene and F127 was set to 0.45 and 1 g, respectively.[88]

The polymer suspension was further centrifuged (Sigma, 3K35) at 10000 rpm and washed several times with ultrapure distilled water until the solution reached pH 7. The polymer was then dried in the freeze dryer (Dieter Piatkowski-Forschungsgeräte, L06) at −50 °C and 10 mbar for 24 h. The dry polymer powder was pyrolyzed at heating rate of 1 °C min^{-1} in a tubular oven (Nabertherm, RHTC80-710/15) at four different T_{Py} of 700, 900, 1100 and 1300 °C in Ar for 3 h.

Carbon synthesis by F127- Aminophenol microwave-assisted hydrothermal route (C_{FAHM})

The reaction solution in FAHM method was prepared similarly to that of FAH method. Thus, a laboratory microwave oven (MLS-MWS Mikrowelle systems, ETHOS Lab) equipped with 12 reaction vials with a capacity of 50 ml each was used and parameters like reaction temperature (RT = 100–140 °C), heating time (HT = 2–20 min) and reaction time (RCT = 1–10 min) were optimized by keeping microwave power at constant value of 1000 W. We assume that reaction mechanism follows via microwave oven method is similar to that of conventional hydrothermal method described in Scheme. 1. After synthesis step, the polymer was pyrolyzed in a tubular oven (Nabertherm, RHTC80-710/15) at temperatures comprised between 700 and 1300 °C.

Characterization of C_{FAH} and C_{FAHM} samples

The surface morphology and the N content of the carbon was analyzed by scanning electron microscopy (SEM) and energy dispersive X-ray spectroscopy (EDX) (Hitachi, FlexSEM 1000 II), respectively. A high-resolution micrograph of carbon and catalyst powders was obtained using transmission electron microscope (TEM) (JEOL, JEM-2011) at 200 kV. Structural analysis of the catalysts was performed by X-ray diffractometer (XRD) (Bruker, D8 Advance) equipped with Cu-α radiation (λ = 0.154 nm) and Raman spectroscopy (Renishaw, inVia confocal Raman Microscope). The thermal stability of the carbon was studied using thermogravimetric analysis (TGA) (Netzsch, Jupiter STH 449). Nitrogen content of carbon was quantified by CHN analyzer (Elementar, Vario MICRO Cube) and X-ray photoelectron spectroscopy (XPS) (Thermo VG Scientific, K-Alpha). Electronic conductivity of carbon powder was measured using a customized cell (Zentrum für Brennstoffzellentechnik, Duisburg, Germany). The instrument consists of pressure piston unit, pressure sensor, vernier caliper, PEEK® sample holder and electrical leads. A desired amount of the powder sample was sandwiched between gold coated stainless steel of 10 mm stubs in a cylindrical PEEK® holder. The maximum volume capacity of PEEK® holder depends on the density of the powder material. The system was designed in such a way that the pressure (P_{max} = 10 bar) can be applied from the top of the stub by piston control (FESTO, ADN-20-25-I-P-A-Q-S2) connected to compressed gas supply. Once the potential was applied (5 mV), the measured current was noted every 5 min until the calibrated force was equivalent to 100 N cm^{-2}. Above this force value, no substantial increase in conductivity was observed. The conductivity value was calculated from Equations (1)–(3):

$$\sigma = \frac{1}{\rho} \tag{1}$$

Where σ is the conductivity and ϱ is the resistivity, which is calculated from the following equation,

$$\rho = \frac{\mathrm{R\ x\ A}}{\mathrm{H}} \tag{2}$$

in which R is the resistance, A the area of the cross section and H the thickness of the sample. R was calculated from ohmic law,

$$\mathrm{R} = \frac{\mathrm{U}}{\mathrm{I}} \tag{3}$$

where U is the applied voltage and I the measured current.

Pt/C synthesis

Pt deposition on as-synthesized carbon (Pt/C) was carried out by impregnating the carbon support with desired amount of hexachloroplatinic acid ($H_2PtCl_6 \cdot 6H_2O$) (Alfa Aesar, 99.99%) followed by a reductive process in 10% methanol-stabilized 37 wt% formaldehyde at 80 °C for 1 h under reflux conditions. The reaction products were washed with ultrapure water and filtered through a 0.4 μm polycarbonate membrane and finally dried in a vacuum oven at 80 °C and 50 mbar for 4 h. The nominal total metal loading on carbon supports was fixed to 40 wt%.

Electrochemical measurements

RRDE experiments

The investigation of Pt/C activity for oxygen reduction reaction (ORR) was performed with a 0.205 cm^2 rotating glassy carbon disk and Pt ring electrode (RRDE, Pine Research Instrumentation). The ink suspension was prepared similar to our earlier work.[29] For the preparation of the ink suspension, 2 mg of Pt/C powder was first

dispersed in a mixture of ultrapure water and isopropanol followed by addition of Nafion solution (5 wt%) into the formed suspension, which were finally loaded onto the electrode. The total catalyst loading of the working electrode was fixed to $80 \pm 10\ \mu g_{Pt}\,cm^{-2}$ for all systems.

A bi-Potentiostat (Pine Research Instrumentation, WaveDrive 20) was used to record the cyclic voltammograms (CV). A Pt wire acted as the counter electrode while a saturated calomel electrode (SCE) (Xylem Analytics GmbH, KE 11-S) was used as reference electrode. The electrochemical surface area (ECSA) of the catalyst was calculated by integrating the hydrogen adsorption region between 0.005 and 0.36 V vs. NHE in the cyclic voltammogram (CV) at $40\ mV\,s^{-1}$ scanning rate and assuming that charge induced by a monolayer of hydrogen atoms on Pt amounts to $210\ \mu C\,cm^{-2}$. Then, Linear Sweep Voltammograms (LSVs) related to Pt/C activity for ORR were recorded in a O_2-saturated 0.5 M H_2SO_4 solution at various speeds from 100 to 2500 rpm and $5\ mV\,s^{-1}$. Accelerated degradation tests (ADT) were carried out in a N_2-saturated electrolyte and consisted of 10,000 cycles in the potential range between 0.4 and 1.4 V at $1\ V\,s^{-1}$. All potential values were normalized to the normal hydrogen electrode (NHE) and are iR-corrected.

GDE experiments

Freshly prepared gas diffusion electrodes (GDE) with a geometric area of $0.5\ cm^2$ were inserted in the GDE cell (Gaskatel, FlexCell®). All experiments were performed with a potentiostat (PARSTAT, PMC-1000) in de-aerated and oxygen-saturated 0.5 M H_2SO_4 at 25 °C. A Pt wire and a reversable hydrogen electrode (RHE) (Gaskatel, HydroFlex®) were employed as the counter and reference electrode, respectively. ADT procedure was carried out in a N_2-saturated electrolyte and consisted of 10,000 cycles in the potential range of 0.4 to 1.4 V at $1\ V\,s^{-1}$. All potential values are normalized to the NHE and iR-corrected.

Acknowledgements

The authors are very grateful for financial support by the "Bundesministerium für Wirtschaft und Energie" (BMWi/19694N). We express our thanks to Mrs. Harling, Saarland University for CHN analysis and Mrs. Klippert, Saarland University for the TEM measurements. We thank Mr. Schäfer, nanoAnalytics for XPS investigation under the "vAW" agreement. We also thank Mrs. Sanchez, DECHEMA-Forschungsinstitut for the BET measurements. Open Access funding enabled and organized by Projekt DEAL.

Conflict of Interest

The authors declare no conflict of interest.

Data Availability Statement

The data that support the findings of this study are available from the corresponding author upon reasonable request.

Keywords: accelerated degradation tests · carbon conductivity · microwave-assisted hydrothermal synthesis · ORR · swelling agent

[1] S. Bose, T. Kuila, T. X. H. Nguyen, N. H. Kim, K.-T. Lau, J. H. Lee, *Prog. Polym. Sci.* **2011**, *36*, 813–843.
[2] S. J. C. Cleghorn, X. Ren, T. E. Springer, M. S. Wilson, C. Zawodzinski, T. A. Zawodinski, S. Gottesfeld, *Int. J. Hydrogen Energy* **1997**, *22*, 1137–1144.
[3] K. B. Prater, *J. Power Sources* **1996**, *61*,105–109.
[4] A. J. Appleby, M. Savy, *J. Electroanal. Chem. Interfacial Electrochem.* **1978**, *92*, 15–30.
[5] M. Oezaslan, F. Hasché, P. Strasser, *J. Electrochem. Soc.* **2012**, *159*, B394.
[6] V. R. Stamenkovic, B. Fowler, B.S Mun, G. Wang, P. N. Ross, C. A. Lucas, N. M. Markovic, *Science* **2007**, *315*, 493–497.
[7] J.-F. Drillet, A. Ee, J. Friedemann, R. Kötz, B. Schnyder, V. M. Schmidt, *Electrochim. Acta* **2002**, *47*, 1983–1988.
[8] M. Sakthivel, I. Radev, V. Peinecke, J.-F. Drillet, *J. Electrochem. Soc.* **2012**, *162*, F901.
[9] V. R. Stamenkovic, B. S. Mun, M. Arenz, K.-J. J. Mayrhofer, C. A. Lucas, G. Wang, P. N. Ross, N. M. Markovic, *Nat. Mater.* **2007**, *6*, 241–247.
[10] V. Stamenkovic, B. S. Mun, K.-J. J. Mayrhofer, P. N. Ross, N. M. Markovic, J. Rossmeisl, J. Greeley, J. K. Nørskov, *Angew. Chem. Int. Ed.* **2006**, *45*, 2963–2967.
[11] J. Wu, S. Shan, H. Cronk, F. Chang, H. Kareem, Y. Zhao, J. Luo, V. Petkov, C.-J. Zhong, *J. Phys. Chem. C* **2017**, *121*, 14128–14136.
[12] P. Trogadas, T. F. Fuller, P. Strasser, *Carbon* **2014**, *75*, 5–42.
[13] J.-F. Drillet, H. Bueb, R. Dittmeyer, U. D-Weglikowska, S. Roth, *J. Electrochem. Soc.* **2009**, *156*, F137.
[14] E. Antolini, *Appl. Catal. B* **2009**, *88*, 1–24.
[15] A. S. Poyraz, C.-H. Kuo, S. Biswas, C. K. King'ondu, S. L. Suib, *Nat. Commun.* **2013**, *4*, 2952.
[16] R. Narayan, U. Y. Nayak, A. M. Raichur, S. Garg, *Pharmaceutica* **2018**, *10*, 118.
[17] D. Banham, F. Feng, K. Pei, S. Ye, V. Birss, *J. Mater. Chem. A* **2013**, *1*, 2812–2820.
[18] M. Sakthivel, J.-F. Drillet, *Appl. Catal. B.* **2018**, *231*, 62–72.
[19] C. Galeano, J. C. Meier, V. Peinecke, H. Bongard, I. Katsounaros, A. A. Topalov, A. Lu, K. J. J. Mayrhofer, F. Schüth, *J. Am. Chem. Soc.* **2012**, *134*, 20457–20465.
[20] A. Vinu, K. Ariga, T. Mori, T. Nakanishi, S. Hishita, D. Golberg, Y. Bando, *Adv. Mater.* **2005**, *17*, 1648–1652.
[21] F. Zhang, Y. Meng, D. Gu, Y. Yan, Z. Chen, B. Tu, D. Zhao, *Chem. Mater.* **2006**, *18*, 5279–5288.
[22] Z. Lei, N. Christov, L. L. Zhang, X. S. Zhao, *J. Mater. Chem.* **2011**, *21*, 2274–2281.
[23] Y. D. Xia, R. Mokaya, *Adv. Mater.* **2004**, *16*, 886–891.
[24] Y. Xie, D. Kocaefe, C. Chen, Y. Kocaefe, *J. Nanomater.* **2016**, *2016*, 1–10.
[25] L. Liu, F.-Y. Wang, G.-S. Shao, T.-Y. Ma, Z.-Y. Yuan, *Carbon* **2010**, *48*, 2660–2664.
[26] A.-H. Lu, B. Spliethoff, F. Schüth, *Chem. Mater.* **2008**, *20*, 5314–5319.
[27] L. Liu, Q.-F. Deng, T.-Y. Ma, X.-Z. Lin, X.-X. Hou, Y.-P. Liu, Z.-Y. Yuan, *J. Mater. Chem.* **2011**, *21*, 16001–16009.
[28] J. Wei, Y. Liang, X. Zhang, G. P. Simon, D. Zhao, J. Zhang, S. Jiang, H. Wang, *Nanoscale* **2015**, *7*, 6247–6254.
[29] H. Javed, S. Pani, J. Antony, M. Sakthivel, J. F. Drillet, *Soft Matter* **2021**, *1*, 7743–7754.
[30] J. Wang, H. Liu, J. Diao, X. Gu, H. Wang, J. Rong, B. Zong, D. S. Su, *J. Mater. Chem. A.* **2015**, *3*, 2305–2313.
[31] Y. Han, S. S. Lee, J. Y. Ying, *Chem. Mater.* **2007**, *19*, 2292–2298.
[32] L. Cao, T. Man, M. Kruk, *Chem. Mater.* **2009**, *21*, 1144–1153.
[33] R. Nagarajan, *Colloids Surf. B* **1999**, *16*, 55–72.
[34] A. Sayari, Y. Yang, M. Kruk, M. Jaroniec, *J. Phys. Chem. B* **1999**, *103*, 3651–3658.
[35] S. Zou, X. Xu, Y. Zhu, C. Cao, *Microporous Mesoporous Mater.* **2017**, *251*, 114–121.
[36] J. Sun, H. Zhang, D. Ma, Y. Chen, X. Bao, A. K-Hoffmann, N. Pfänder, D. S. Su, *Chem. Commun.* **2005**, *42*, 5343–5345.
[37] L. Huang, X. Yan, M. Kruk, *Langmuir* **2010**, *26*, 14871–14878.
[38] M. Mandal, M. Kruk, *Chem. Mater.* **2012**, *24*, 123–132.
[39] K. K. R. Datta, V. V. Balasubramanian, K. Ariga, T. Mori, A. Vinu, *Eur. J. Chem.* **2011**, *17*, 3390–3397.
[40] P. Stonehart, *Phys. Chem.* **1990**, *94*, 913–921.
[41] Y. Xia, Z. Yang, R. Mokaya, *Stud. Surf. Sci. Catal.* **2005**, *156*, 565–572.

[42] R. I. Jafri, N. Rajalakshmi, S. Ramaprabhu, *J. Mater. Chem.* **2010**, *20*, 7114–7117.
[43] X.-K. Kong, C.-Le. Chen, Q.-W. Chen, *Chem. Soc. Rev.* **2014**, *43*, 2841–2857.
[44] K. Gong, F. Du, Z. Xia, M. Durstock, L. Dai, *Science* **2009**, *323*, 760–764.
[45] S. Liu, P. Zuo, Y. Wang, X. Li, W. Zhang, S. Xu, P. Huo, Z. Li, *Microporous Mesoporous Mater.* **2018**, *259*, 54–59.
[46] D. Wei, Y. Liu, Y. Wang, H. Zhang, L. Huang, G. Yu, *Nano Lett.* **2009**, *9*, 1752–1758.
[47] A. Y. Liu, M. L. Cohen, *Science* **1989**, *245*, 841–842.
[48] A. J. Stevens, T. Koga, C. B. Agee, M. J. Aziz, C. M. Lieber, *J. Am. Chem. Soc.* **1996**, *118*, 10900–10901.
[49] Z. X. Wu, P. A. Webley, D. Y. Zhao, *J. Mater. Chem.* **2012**, *22*, 11379–11389.
[50] T. Zhou, Y. Zhou, R. Ma, Z. Zhou, G. Liu, Q. Liu, Y. Zhu, J. Wang, *Carbon* **2017**, *114*, 177–186.
[51] Y. Shao, Z.-Y Hu, Y. Yao, X.-R. Wei, X.-M. Gao, Z.-X. Wu, *New. Carbon. Mater.*r. **2022**, *37*, 259–276.
[52] S. Zhou, S. Deng, Z. Wang, W. Liao, M. Chen, Q. Wang, *ENFUEM.* **2021**, *35*, 20300–20308.
[53] X. Xie, C. He, B. Li, Y. He, D. A. Cullen, E. C. Wegener, A. J. Kropf, U. Martinez, Y. Cheng, M. H. Engelhard, M. E. Bowden, M. Song, T. Lemmon, X. S. Li, Z. Nie, J. Liu, D. J. Myers, P. Zelenay, G. Wang, G. Wu, V. Ramani, Y. Shao, *Nat. Catal.* **2020**, *3*, 1044–1054.
[54] D. M. P. Mingos, D. R. Baghurst, *Chem. Soc. Rev.* **1991**, *20*, 1–47.
[55] R. Gedye, F. Smith, K. Westaway, H. Ali, L. Baldisera, L. Laberge, J. Rousell, *Tetrahedron Lett.* **1986**, *27*, 279–282.
[56] C. R. Strauss, R. W. Trainor, *Aust. J. Chem.* **1995**, *48*, 1665–1692.
[57] F. Langa, P. D. L. Cruz, A. D. L. Hoz, A. Díaz-Ortiz, E. Díez-Barra, *Contemp. Org. Synth.* **1997**, *4*, 373–386.
[58] C.-G. Wu, T. Bein, *Chem. Commun.* **1996**, *8*, 925–926.
[59] L. Chen, X. Cui, M. Wang, Y. Du, X. Zhang, G. Wan, L. Zhang, F. Cui, C. Wei, J. Shi, *Langmuir* **2015**, *31*, 7644–7651.
[60] Y. Liu, L. Pan, T. Chen, X. Xu, T. Lu, Z. Sun, D. H. C. Chua, *Electrochim. Acta* **2015**, *151*, 489–496.
[61] H. I. Lee, J. H. Kim, S. H. Joo, H. Chang, D. Seung, O. Joo, D. J. Suh, W. Ahn, C. Pak, J. M. Kim, *Carbon* **2007**, *45*, 2843–2854.
[62] A. F. Arif, Y. Kobayashi, R. Balgis, T. Ogi, H. Iwasaki, K. Okuyama, *Carbon* **2016**, *107*, 11–19.
[63] F. Wiesbrock, R. Hoogenboom, U. S. Schubert, *Macromol. Rapid Commun.* **2004**, *25*, 1739–1764.
[64] J. Tao, L. Xu, L. Wan, J. Hou, P. Yi, P. Chen, J. Zhou, Z. Yao, *Nanoscale* **2021**, *13*, 12896–12909.
[65] Y. Liu, L. Pan, T. Chen, X. Xu, T. Lu, Z. Sun, D. H. C. Chua, *Electrochim. Acta* **2015**, *151*, 489–496.
[66] Y. Zhai, Y. Dou, X. Liu, S. S. Park, C.-S. Ha, D. Zhao, *Carbon* **2011**, *49*, 545–555.
[67] B. Bayatsarmadi, Y. Zheng, M. Jaroniec, S. Z. Qiao, *Chem. Asian J.* **2015**, *10*, 1546–1553.
[68] X. Liu, Y. Zhou, C.-L. Wang, Y. Liu, D.-J. Tao, *Chem. Eng. J.* **2022**, *427*, 130878.
[69] A. Heckmann, P. Meister, H.-W. Meyer, A. Rohrbach, M. Winter, T. Placke, *ECS Trans.* **2015**, *66*, 1–12.
[70] X. Kan, X. Chen, W. Chen, J Mi, J.-Y. Zhang, F. Liu, A. Zheng, K. Huang, L. Shen, C. Au, L. Jiang, *ACS Sustainable Chem. Eng.* **2019**, *7*, 7609–7618.
[71] W. Qi, W. Li, B. Zhang, X. Gu, X. Guo, D. Su, *Angew. Chem. Int. Ed.* **2013**, *52*, 14224–14228; *Angew. Chem.* **2013**, *125*, 14474–14478.
[72] E. Frackowiak, K. Jurewicz, K. Szostak, S. Delpeuxa, F. Béguin, *Fuel Process. Technol.* **2002**, *77–78*, 213–219.
[73] C. Nie, L. Pan, H. Li, T. Chen, T. Lu, Z. Sun, *J. Electroanal. Chem.* **2012**, *666*, 85–88.
[74] Y. Jia, L. Zhang, A. Du, G. Gao, J. Chen, X. Yan, C. L. Brown, X. Yao, *Adv. Mater.* **2016**, *28*, 9532–9538.
[75] C. Zhang, N. Mahmood, H. Yin, F. Liu, Y. Hou, *Adv. Mater.* **2013**, *25*, 4932–4937.
[76] A. K. Sircar, T. G. Lamond, *Rubber Chem. Technol.* **1978**, *51*, 126–132.
[77] S. Yang, X. Feng, X. Wang, K. Müllen, *Angew. Chem. Int. Ed.* **2011**, *50*, 5451–5455.
[78] K. E. Swider, D. R. Rolison, *J. Electrochem. Soc.* **1996**, *143*, 813.
[79] L. G. Bulusheva, V. E. Arkhipov, K. M. Popov, V. I. Sysoev, A. A. Makarova, A. V. Okotrub, *Materials* **2020**, *13*, 1173.
[80] D. Guo, R. Shibuya, C. Akiba, S. Saji, T. Kondo, J. Nakamura, *Science* **2016**, *351*, 361–365.
[81] K. Parvez, S. Yang, Y. Hernandez, A. Winter, A. Turchanin, X. Feng, K. Müllen, *ACS Nano* **2012**, *6*, 9541–9550.
[82] J. Gao, Y. Wang, H. Wu, X. Liu, L. Wang, Q. Yu, A. Li, H. Wang, C. Song, Z. Gao, M. Peng, M. Zhang, N. Ma, J. Wang, W. Zhou, G. Wang, Z. Yin, D. Ma, *Angew. Chem.* **2019**, *131*, 15089–15097.
[83] G. Zhong, S. Xu, L. Liu, C. Z. Zheng, J. Dou, F. Wang, X. Fu, W. Liao, H. Wang, *ChemElectroChem.* **2020**, *7*, 1107–1114.
[84] S. S. Shinde, C. H. Lee, A. Sami, D. H. Kim, S. U. Lee, J. H. Lee, *ACS Nano* **2017**, *11*, 347–357.
[85] J. Wang, C.-X. Zhao, J.-N. Liu, D. Ren, B.-Q. Li, J.-Q. Huang, Q. Zhang, *Nano Mater. Sci.* **2021**, *3*, 313–318.
[86] Q. Lv, W. Si, J. He, L. Sun, C. Zhang, N. Wang, Z. Yang, X. Li, X. Wang, W. Deng, Y. Long, C. Huang, Y. Li, *Nat. Commun.* **2018**, *9*, 3376.
[87] U. A. Paulus, T. J. Schmidt, H. A. Gasteiger, R. J. Behm, *J. Electroanal. Chem.* **2001**, *495*, 134–145.
[88] A. S. Machanda, M. Kruk, *Microporous Mesoporous Mater.* **2016**, *222*, 153–159.

Manuscript received: December 7, 2022
Revised manuscript received: January 20, 2023
Accepted manuscript online: February 3, 2023
Version of record online: February 24, 2023